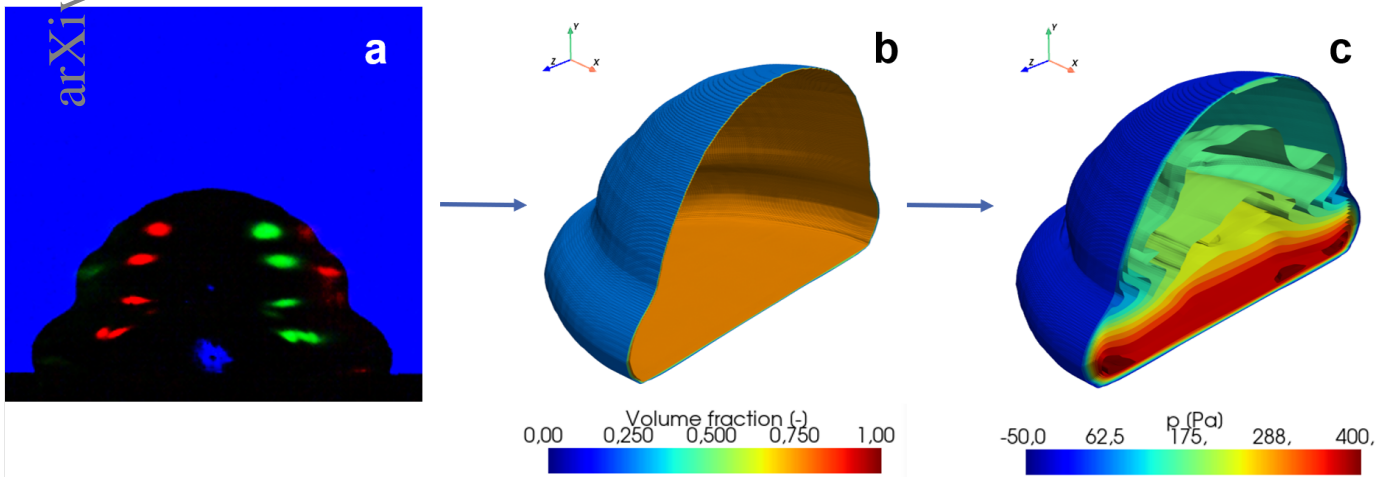


Graphical Abstract

PINNs4Drops: Convolutional feature-enhanced physics-informed neural networks for reconstructing two-phase flows

Maximilian Dreisbach, Elham Kiyani, Jochen Kriegseis, George Karniadakis, Alexander Stroh



Graphical abstract: (a) Image of an impinging droplet recorded in the experiments, (b) Iso-contours of the inferred volume fraction distribution, (c) Iso-contours of the inferred pressure distribution.

PINNs4Drops: Convolutional feature-enhanced physics-informed neural networks for reconstructing two-phase flows

Maximilian Dreisbach^a, Elham Kiyani^b, Jochen Kriegseis^a, George Karniadakis^c, Alexander Stroh^a

^a*Institute of Fluid Mechanics, Karlsruhe Institute of Technology, Kaiserstraße 10, Karlsruhe, 76131, Germany*

^b*Division of Applied Mathematics, Brown University, Providence, 02912, RI, USA*

^c*Division of Applied Mathematics and School of Engineering, Brown University, Providence, 02912, RI, USA*

Abstract

Two-phase flow phenomena play a key role in many engineering applications, including hydrogen fuel cells, spray cooling techniques and combustion. Specialized techniques like shadowgraphy and particle image velocimetry can reveal gas-liquid interface evolution and internal velocity fields; however, they are largely limited to planar measurements, while flow dynamics are inherently three-dimensional (3D). Deep learning techniques based on convolutional neural networks provide a powerful approach for volumetric reconstruction based on the experimental data by leveraging spatial structure of images and extracting context-rich features. Building on this foundation, Physics-informed neural networks (PINNs) offer a complementary and promising alternative integrating prior knowledge in the form of governing equations into the networks training process. This integration enables accurate predictions even with limited data. By combining the strengths of both approaches, we propose a novel convolutional feature-enhanced PINNs framework, designed for the spatio-temporal reconstruction of two-phase flows from color-coded shadowgraphy images. The proposed approach is first validated on synthetic data generated through direct numerical simulation, demonstrating high spatial accuracy in reconstructing the three-dimensional gas-liquid interface, along with the inferred velocity and pressure fields. Subsequently, we apply this method to interface reconstruction for an impinging droplet using planar experimental data, highlighting the practical applicability and significant potential of the proposed approach to real-world fluid dynamics analysis.

Keywords: two-phase flow, interfacial dynamics, physics-informed neural networks, volumetric reconstruction, deep learning

1. Introduction

Two-phase flows, involving liquid droplets or gaseous bubbles, are ubiquitous in nature and technology. In particular, liquid droplets in a gaseous environment are critical in a variety of technical applications. These include the impingement of liquid droplets on wet or dry surfaces, such as in spray cooling [1], spray coating [2, 3], inkjet printing [4], and adhering droplets in external flows for applications like cleaning and drying [5, 6], oil recovery [7, 8, 9, 10], heat exchangers [11, 12], airfoil icing prevention [13], and fuel cells, where efficient removal of water droplets is essential for optimal performance [14, 15, 16, 17]. These problems involve moving gas-liquid interfaces, which induce internal flow within the droplet and can result in complex interactions between the internal and external flows and the interface. Common measurement techniques employed for the experimental investigation of droplet flows include shadowgraphy, used to obtain the interface location, and Particle Image Velocimetry (PIV) for the measurement of velocity fields. Shadowgraphy is particularly favoured for the reconstruction of the three-dimensional gas-liquid interface due to its simplicity and high spatial accuracy.

However, to capture the complex three-dimensional deformation of the interface, which may involve non-convex shapes and self-occlusion, multiple camera angles are typically required [18, 19]. Limited optical access in many applications,

however, makes the development of single-view reconstructing techniques highly desirable. PIV is commonly utilized to study internal droplet flows. Previous studies have shown how PIV can be used to reveal complex flow patterns influenced by factors such as interfacial tension, Marangoni effects [20, 21], and interface oscillation [22, 23] in scenarios like freezing [13], flow in microchannels [24], and liquid-liquid dispersion [25]. However, the refraction of light at the gas-liquid interface distorts the measured velocity field, requiring complex correction procedures [26, 27] and precise knowledge of the instantaneous three-dimensional (3D) interface shape.

Numerical simulations are increasingly used for the investigation of droplet flows [28, 29, 30]. While these simulations can accurately predict the three-dimensional dynamics of droplets, they are often computationally expensive and limited to idealized cases. Moreover, modelling surface tension effects and contact angle dynamics remains challenging, often relying on experimental data for validation or model refinement [31, 32]. Therefore, extracting three-dimensional data from experiments is crucial for gaining deeper insight into two-phase dynamics. Previously, Dreisbach et al. [33] employed data-driven reconstruction techniques based on convolutional neural networks (CNNs) [34] for the accurate reconstruction of the interface dynamics during droplet impingement from monocular optical experiments. However, the underlying laws of physics governing the two-phase flow are only implicitly learned from

numerical data and the reconstruction of individual morphological instances does not consider the temporal coherence of the droplet dynamics, which limits the reconstruction accuracy. Here, physics-informed neural networks (PINNs) Raissi et al. [35] approach is anticipated to enhance the learning of spatio-temporal droplet dynamics by incorporating both these untapped sources of prior knowledge into the reconstruction.

PINNs have emerged as a powerful framework for solving complex problems by seamlessly integrating governing equations into the data-driven approach. Their expressivity in approximating non-linear functions, combined with their unified framework for solving both forward and inverse problems, makes the PINN approach particularly well-suited for tackling fluid mechanical challenges [36, 37, 38, 39, 40]. PINNs have been applied to encode the continuity equation and the non-dimensional incompressible Navier-Stokes equations (NSE). This approach has been used to address the inverse problems in the flow past a circular cylinder; for example, the data-driven discovery of the viscosity in unknown fluids and the inference of the unknown hidden states, particularly, the continuous pressure field from scattered velocity observations.

Jin et al. [41] employed PINNs to simulate a 3D turbulent channel flow at $Re_\tau = 1,000$ by training a neural network on the NSE with specified velocity boundary and initial conditions. They addressed the challenge of ill-posed problem arising from partially missing or noisy boundary conditions, demonstrating that PINNs can still yield accurate solutions under such circumstances. Similarly, Xu et al. [42] extended the application of PINNs to identify artificial viscosity in parametric turbulent incompressible NSE, leveraging dataset from 2D turbulent flow simulations. Furthermore, the authors demonstrated that PINNs can accurately reconstruct both laminar and turbulent flow fields in regions of the domain where no measurement data is available, addressing challenges such as low fidelity or experimental limitations. Expanding on this capability, Cai et al. [36] employed PINNs to reconstruct the 3D velocity and pressure fields in the unsteady wake flow past a circular cylinder at $Re = 200$ using 2D two-component (2D2C) velocity observations. Motivated by the potential application in the post-processing of particle image velocimetry measurements, they showed that as few as four cross-planes of 2D2C data are sufficient to accurately reconstruct the continuous 3D velocity and pressure fields, even without initial or boundary conditions. Raissi et al. [43] demonstrated the ability of PINNs to predict quantitatively accurate continuous 3D velocity and pressure fields from measurements of the tracer particle concentration. This was achieved without requiring any data, boundary or initial conditions for the quantities of interest by training PINNs on NSE, the continuity equation, and the transport equation for the passive scalar of the concentration. Additionally, the authors showed that PINNs could estimate derived quantities, such as shear forces and vorticity fields since exact gradients of the solution can be calculated at all points in the domain and at any desired resolution. Building on this concept, Cai et al. [44] extended the hidden fluid mechanics approach [43] to reconstruct continuous 3D velocity and pressure fields from 3D temperature measurements. By training PINNs on the Boussinesq

approximation of the incompressible Navier-Stokes equations, the heat transfer equation, and the measured temperature data, they successfully analyzed the buoyancy-driven flow over an espresso cup, showcasing the versatility of PINNs in handling diverse fluid mechanics problems. Furthermore, the authors demonstrated that PINNs are robust to noise and low-resolution training data in both the spatial and temporal domains, enabling the reconstruction of latent variables at a higher spatio-temporal resolution than the experimental data. Mao et al. [45] applied PINNs to compressible 2D flows governed by the Euler equations to reconstruct velocity, pressure and density field in high-speed aerodynamic flows, using measurements of the density gradient in analogy to Schlieren experiments. They highlighted the importance of the spatial distribution of the sampling points, particularly for problems involving discontinuities in the flow fields. To address this, the authors proposed adaptive sampling strategies that dynamically track the discontinuities during training, increasing sampling density in critical regions based on the residuals of the PDEs or the gradients of the predicted solution. Building on these advancements, Wang and Perdikaris [46] introduced a multi-network PINNs framework to tackle the partial differential equations (PDEs) involving dynamic interfaces and phase change phenomena. In their approach, one neural network is trained to approximate the temperature field, while a second network parameterized the unknown and moving interfaces. These networks were coupled through a physics-informed network that encodes the corresponding heat transfer equation.

The application of PINNs for two-phase flows necessitates specialized treatment of the interface, as the approximation of the discontinuity at the interface can result in steep solution gradients and locally high errors, potentially hindering optimisation and even preventing convergence of the method. To address these challenges, Buhendwa et al. [47] extended the concept of hidden fluid mechanics framework to predict continuous 2D velocity and pressure fields for incompressible two-phase flows from auxiliary information about interface position. Following the Volume of Fluid (VoF) approach, the PINNs are trained on the residual of the dimensionless single-field Navier-Stokes equations, the continuity equation, and the advection equation for the volume fraction α , alongside a data loss term for the interface position. By implementing local refinement of the residual and data points near the interface, the optimisation process was effectively focused on the region of the domain with the highest residuals, significantly stabilizing learning and reducing solution errors [48]. Moreover, appropriate weighting of the loss terms, particularly the momentum equation residuals, was crucial to prevent divergence of the optimisation caused by abrupt changes in the magnitude of the surface tension term. Building on this work, Qiu et al. [49] developed PINNs using the phase-field method to simulate 2D incompressible two-phase flows with large density ratios up to 1,000 between the the phases. They noted that the VoF approach as proposed by Buhendwa et al. [47] encountered stability issues at high density ratios due to the non-zero divergence of the velocity field at the interface. Previously, Buhendwa et al. [47] successfully addressed similar two-phase flows with den-

sity ratio ratios up to 10. Building on this, Qiu et al. [49] trained PINNs on a physics-informed loss incorporating the residuals of the continuity equation, the momentum equations as well as the Cahn-Hilliard equation to capture the interface evolution. This was combined with loss terms for the initial and boundary conditions for both the velocity and phase indicator variable. Expanding the scope of interfacial problems, Chen et al. [50] employed PINNs to solve the coupled Cahn-Hilliard and Allen-Cahn equations within the context of the phase-field method to simulate interfacial problems related to various phenomena related to electrochemical corrosion. Dynamic interfaces were addressed using adaptive sampling strategies based on the residuals of the PDEs or the gradients of the solution, as suggested by Mao et al. [45], which significantly enhanced prediction accuracy. Furthermore, an adaptive weighting scheme based on the convergence rate of the individual loss terms was employed to balance contributions of the coupled PDEs and the initial and boundary conditions [51]. This approach significantly improved the accuracy for predicting the location of the dynamic interface.

The present work introduces a novel convolutional feature-enhanced PINN framework for the spatio-temporal reconstruction of the gas-liquid interface along with the three-dimensional velocity and pressure fields in two-phase flows. The methodology utilizes monocular recordings obtained through a purposefully developed optical measurement technique based on shadowgraphy and color-coded glare points. The paper is organized as follows. In section 2, we present the methodology both for PINNs and measurements, in section 3 we present the results with a discussion and we summarize in section 4. In the appendix, we include additional results to quantify the errors of the new method.

2. Methodology

In the present work, the Pixel-Aligned Implicit Function (PIFu)-approach [34] for the volumetric reconstruction of the gas-liquid interface is extended by the integration of physics-informed losses by which the single-field two-phase formulation of the Navier-Stokes equations, the continuity equation and the equation for the interface evolution are encoded in the neural network. The continuity and Navier-Stokes equations are harnessed to learn the dynamics of the two-phase flow, while the interface evolution equation is employed to couple the velocity field to the distribution of the two phases and, consequently, the location of the gas-liquid interface. The representation of the gas-liquid interface as a continuous implicit function through a neural network in the PIFu-approach is more akin to diffuse interface methods than sharp interface methods. Moreover, the physically sound modelling of the interface dynamics in the phase-field approach renders the method promising for accurate predictions of two-phase flows at high density and viscosity ratios, as demonstrated recently by Qiu et al. [49]. Therefore, the convective Cahn-Hilliard equation (eq. (7)) appears as a highly suitable choice for representing the interface evolution. However, computing the physics-informed loss derived from

the Cahn-Hilliard equation ((7)) involves fourth-order derivatives, when coupled with the complexity of three-dimensional domain, significantly increases computational demands. Furthermore, the repeated calculation of gradients through automatic differentiation to obtain the fourth-order derivatives leads to the accumulation of potential errors. In contrast, the VoF approach offers a simplified alternative by representing the interface evolution through the transport equation for the volume fraction, which is purely convective and thus it involves only first-order derivatives. The successful application of PINNs based on the VoF method to inverse two-phase flow problems, as demonstrated by Buhendwa et al. [47], highlights the feasibility and efficiency of this approach for tackling such problems. However, the applicability of PINNs in the VoF formulation for two-phase flows at high density ratios remains unverified. To address this, we will develop two variants of PINNs, one based on the phase-field method (*PF-PINNs-vI*) and the other on VoF (*VOF-PINNs*). These variants will share the same neural network architecture and will be comparatively evaluated to assess their performance.

The computation of the physics-informed loss terms using automatic differentiation requires predictions of the three-dimensional velocity and pressure fields, necessitating modifications to the network architecture. Specifically, the output layer of the network must be extended to predict three velocity components u , v , and w , as well as the pressure p . Additionally, the input layer must be adapted to include the spatio-temporal coordinates x , y , z , and time t to enable the computation of the derivatives of the predicted quantities.

Figure 1 illustrates the network architecture of the proposed PINN, which consists of three major components, namely, the feature extraction network (a CNN), the neural network (a multi-layer perceptron (MLP)), and the physics-informed network. First, the glare-point shadowgraphy images are processed using a convolutional hourglass network [52], which extracts pixel-aligned features I_i from the input image at the location x, y on the image plane. The extracted image features along with their corresponding spatial coordinates x, y are forwarded to an MLP. Additionally, the temporal coordinate t and the spatial coordinate z are given as inputs to the MLP. The MLP predicts the phase distribution ϕ , the three components of the velocity vector $\mathbf{u} = (u, v, w)^T$, as well as the pressure p at x, y, z, t . The residuals of the single-field two-phase Navier-Stokes, continuity and interface evolution equations are computed using automatic differentiation applied to the predicted output with respect to the spatio-temporal input coordinates. These residuals form the basis for physics-informed loss terms, i.e., the continuity equation (L_{Conti}), the advection equation governing the interface (L_{Adv}) and the Navier-Stokes momentum equations ($L_{NSE,j}$), with $j = (x, y, z)$. Each loss term is defined as the mean squared error (MSE) of the respective residuals. In addition to these physics-informed losses, ground truth labels for the velocity and pressure fields, as well as surface meshes of the gas-liquid interface, are extracted from numerical simulations. These labels are used to define data loss terms for the predicted quantities ϕ, u, v, w, p , computed as the MSE between the predictions and ground truth. The joint neural networks are

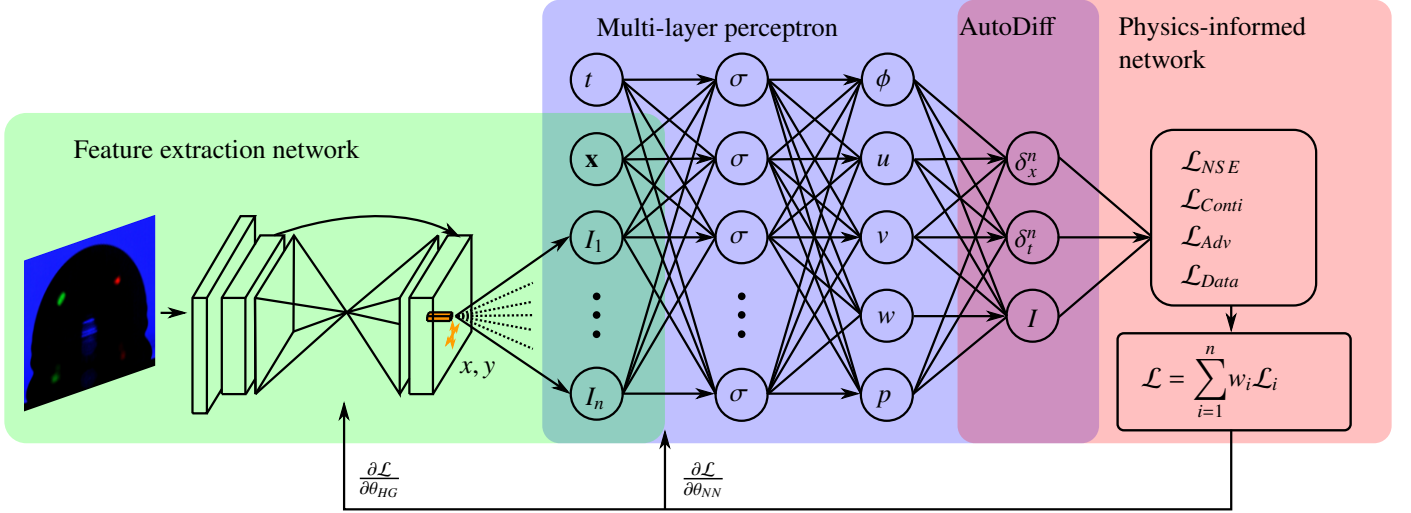


Figure 1: Schematic of the Convolutional Feature-Enhanced PINN Framework architecture. The proposed PINNs4Drops framework predicts the three-dimensional gas-liquid interface and the velocity and pressure distributions. Initially, glare-point shadowgraphy images are processed using a convolutional hourglass network, which extracts pixel-aligned features from the input image at the pixel location (x, y) on the image plane. These extracted features, along with the temporal coordinate t and the spatial coordinate z , are provided as inputs to an MLP. The MLP predicts the phase distribution ϕ , the three components of the velocity vector $\mathbf{u} = (u, v, w)^T$, and the pressure p at the spatio-temporal coordinates (x, y, z, t) . The loss function comprises a data loss term and physics-informed loss terms. The physics-informed loss terms enforce the governing equations and are defined as the MSE of the following residuals: L_{Conti} , enforcing the continuity equation; L_{Adv} , representing the advection equation for phase distribution ϕ ; and $L_{NSE,j}$, representing the Navier-Stokes equations for momentum conservation, with $j = (x, y, z)$ indicating the spatial components.

trained on a composite loss representing the weighted sum of the physics-informed loss terms and the data loss terms

$$L = \sum_{i=1}^n w_i L_i = w_\phi L_\phi + w_u L_u + w_v L_v + w_w L_w + w_p L_p + w_{Conti} L_{Conti} + w_{Adv} L_{Adv} + w_{NSE,x} L_{NSE,x} + w_{NSE,y} L_{NSE,y} + w_{NSE,z} L_{NSE,z} \quad (1)$$

The formulation of governing equations, dedicated sampling schemes, and particular design choices for the neural network architecture play a critical role in the successful application of PINNs for two-phase flow problems. The methods employed for the proposed PINNs will be detailed in the following sections.

2.1. Governing equations

It has been shown that the computation of the physics-informed losses based on the dimensionless formulation of the Navier-Stokes equations results in moderately improved accuracy of the predicted flow quantities compared to the dimensional formulation [44]. Furthermore, the similar magnitude of the dimensionless PDE terms facilitate the balancing of different physics-informed loss components [53]. Therefore, the dimensionless single-field Navier-Stokes equations are employed

$$\rho^* \left(\frac{\partial \mathbf{u}^*}{\partial t^*} + (\mathbf{u}^* \cdot \nabla^*) \mathbf{u}^* \right) = -\nabla^* p^* + \nabla^* \cdot \left(\frac{1}{\text{Re}} (\nabla^* \mathbf{u}^* + \nabla^{*T} \mathbf{u}^*) \right) + \frac{1}{\text{We}} \frac{\mathbf{f}_\sigma}{\sigma} + \rho^* \frac{1}{\text{Fr}^2} \quad (2)$$

with the following relationships between dimensional and non-dimensional quantities for the velocity $\mathbf{u} = \mathbf{u}^* u_R$, the pressure $p = p^* \rho_R u_R^2$, the density $\rho = \rho^* \rho_R$, the spatial coordinates $\mathbf{x} = \mathbf{x}^* L_R$, and the time $t = t^* L_R / u_R$, as well as the Reynolds number $\text{Re} = \rho_R u_R L_R / \mu$, Weber number $\text{We} = \rho_R u_R^2 L_R / \sigma$, and Froude number $\text{Fr} = u_R / \sqrt{\mathbf{g} L_R}$. The dynamic viscosity, surface tension coefficient and gravitational acceleration are indicated by μ , σ and \mathbf{g} , respectively. The reference quantities are the impact velocity $u_R = u_0$ for the considered case of droplet impingement, the density of the liquid phase $\rho_R = \rho_L$ and the reproduction scale $L_R = r_p$ of the computational domain to the experiments, which ensures the correct scaling of the surface curvature required for the calculation of surface tension. Both versions of the PINNs employ the continuity equation for incompressible fluids

$$\nabla \cdot \mathbf{u}^* = 0. \quad (3)$$

Volume of Fluid-based Physics-Informed Neural Networks (VoF-PINNs) represent the interface evolution in two-phase flows using the Volume of Fluid (VoF) method, a well-established approach for capturing fluid interfaces. The transport equation for the volume fraction α is employed to describe the interface evolution, following the formulation of algebraic VoF approaches [54].

$$\frac{\partial \alpha}{\partial t} + (\mathbf{u}^* \cdot \nabla) \alpha = 0. \quad (4)$$

The volume fraction α indicates whether a computational cell is occupied by the liquid ($\alpha = 1$), the gaseous phase ($\alpha = 0$), or both ($0 < \alpha < 1$). The surface tension f_σ is modelled using the Continuum Surface Force (CSF) model [55] as a localised

body force within the transition region of finite thickness at the interface

$$\mathbf{f}_\sigma = -\sigma\kappa\nabla\alpha \quad (5)$$

where σ is the surface tension coefficient, and κ is the cell-averaged curvature of the interface. The curvature of the interface is approximated by $\kappa = -\nabla \cdot \mathbf{n}_i$ with the outwards pointing normal vector of the liquid interface \mathbf{n}_i , which is represented by the gradient of the volume fraction $\mathbf{n}_i = \frac{\nabla\alpha}{|\nabla\alpha|}$. The mixture density ρ and viscosity μ are determined by the arithmetic mean of the fluid properties in both phases

$$\xi = \alpha\xi_l + (1 - \alpha)\xi_g \quad \text{with} \quad \xi \in \{\rho, \mu\}. \quad (6)$$

The phase-field version employs the convective Cahn-Hilliard equation [56] to represent interface evolution,

$$\frac{\partial C}{\partial t} + (\mathbf{u}^* \cdot \nabla) C = M\nabla^2\psi \quad (7)$$

with the mobility parameter M that determines the relaxation time of the interface and the conserved order parameter C that represents both phases and takes the value of $C_l = 1$ in the liquid phase and $C_g = -1$ in the gaseous phase. According to the diffuse-interface theory [57] the phase separation and diffusion in two-phase flows are driven by the chemical potential at the interface ψ , which is derived as the variational derivative of the mixing energy with respect to the order parameter C

$$\psi = \frac{\delta F_{mix}}{\delta C} = \frac{\lambda}{\epsilon^2} C(C^2 - 1) - \lambda\nabla^2 C, \quad (8)$$

where λ represents the magnitude of the mixing energy and ϵ is the capillary width, which is proportional to the interface thickness equating the surface energy and the mixing energy in the interface region yields [58]

$$\sigma = \frac{2\sqrt{2}}{3} \frac{\lambda}{\epsilon}. \quad (9)$$

As the surface tension coefficient σ can be measured by experiments, equation 9 can be used to determine the mixing energy λ . The value for ϵ , however, needs to be chosen and is typically defined in relation to the characteristic macroscopic length scale of the flow. In the phase-field version, the continuum surface tension in the potential form [59] is employed

$$\mathbf{f}_\sigma = \psi\nabla C. \quad (10)$$

The mixture density ρ and viscosity μ are determined as

$$\xi_M = \frac{1+C}{2}\xi_l + \frac{1-C}{2}\xi_g \quad \text{with} \quad \xi \in \{\rho, \mu\}. \quad (11)$$

In the phase-field PINNs, referred to as *PF-PINNs-v1*, the capillary width ϵ is treated as a learnable parameter. In order to promote the convergence toward a thin interface, an additional loss term is introduced, defined as the Huber loss [60] between ϵ and the value of $\epsilon_l = 2.2 \cdot 10^5$, determined by Fink et al. [28]. The capillary width ϵ is initialised with values ranging from 0.01 to 0.05 to study the influence of the parameter and

the weight for the additional learnable interface loss is set to $w_\epsilon = 100$. To address potential issues arising from the fourth-order derivatives in the Cahn-Hilliard equation employed for the phase-field version of the PINNs, a second variant of phase-field PINNs is proposed. This variant, referred to as *PF-PINNs-v2*, the chemical potential ψ is directly predicted using the neural network, in contrast to the computation of ψ from C in *PF-PINNs-v1*, reducing the highest order of derivatives to the second order. An additional loss term is derived from the residual of equation 8, to ensure the consistency between the predicted phase distribution and the distribution of the chemical potential. This provides additional supervision for the learning of ψ . The weight for this additional identity loss of the chemical potential is set to $w_\psi = 0.1$.

Previous research has demonstrated the critical role of proper loss weighting to achieve the simultaneous convergence of all loss terms [47, 53, 51]. To address this, a combination of fixed loss weights and adaptive loss weighting is used to balance the data-driven and physics-informed loss terms during training. For the inverse problem of the flow field reconstruction in a flow with natural convection, larger relative weights for the data loss terms compared to the physics-informed losses have been shown to be beneficial [44]. Furthermore, the accurate prediction of the phase distribution is crucial for correctly computing the momentum equation, as the mixture density ρ_M significantly affects the momentum balance. Optimal weights for achieving the simultaneous convergence of all loss terms were determined experimentally as $w_{u,v,w,p} = 10$, $w_{Conti,adv,NSE,x} = 1,000$, $w_{NSE,y} = 1$ and $w_{NSE,z} = 100$. These weights yielded weighted physics-informed and data loss terms for u, v, w, p that ranged between one and three orders of magnitude lower than the weighted loss for the phase distribution. In addition to using the fixed loss weights, the adaptive loss weighting scheme *SoftAdapt* [61] was employed to dynamically balance the loss terms during training. This simple loss weighting scheme is based on the relative convergence rate of the different loss terms, with inversely proportional loss weights determined dynamically. *SoftAdapt* significantly improves training dynamics and enhances the accuracy of the trained model, all while incurring minimal computational costs. Both fixed and adaptive loss weights were applied in a multiplicative manner. Given the importance of the phase distribution for the physics-informed loss terms, it is essential that the optimization process ensures the accurate convergence of the phase distribution prediction before introducing the physics-informed losses. Therefore, the neural network was initially trained only on the data loss terms until the data L_ϕ decreased below a specified threshold $L_{\phi,T}$. Once this threshold was reached, the physics-informed losses were incorporated into the weighted composite loss. A threshold value $L_{\phi,T} = 0.03$ was determined to provide a sufficient convergence of the prediction for the phase distribution to obtain adequate physics-informed losses. Additionally, the data loss terms for u, v, w, p were gradually increased during the first 5,000 training iterations by an additional weighting factor, which scaled linearly from zero to one from training iteration zero to 5,000 to prioritise the learning of an accurate interface prediction in the early stages of training.

2.2. Sampling methods

Previous studies have demonstrated that an adaptive refinement of the sampling points for the loss computation at the gas-liquid interface is essential for the successful application of PINNs to two-phase flow problems [47, 50]. This necessity arises from the steep gradients of the solution near the interface [45, 48], which require higher sampling density to accurately capture the physics in these regions. Therefore, a combination of adaptive and random sampling at a ratio of 16 : 1 is employed. The dense adaptive sampling near the interface facilitates the learning of an accurately localized prediction for the gas-liquid interface, while few random sampling points across the rest of the domain are required to prevent overfitting. Following the adaptive surface sampling method introduced by Saito et al. [34], random sampling from a normal distribution centered on the interface with a standard deviation $\sigma = 3.9\%$ of the domain size is used to refine the sampling points near the interface. This corresponds to an adaptive sampling at a thickness of 0.107 mm near the interface in physical space or 5% of droplet diameter $d_0 = 2.1$ mm, respectively. The data loss terms and the physics-informed loss terms are calculated on different sets of sampling points in order to effectively exploit the continuous nature of PINNs, which allows for the computation of residuals at any sampling point in the spatio-temporal domain. Thereby, prior knowledge from the numerical simulation is incorporated into the PINNs through supervised learning, while further residual sampling points at different locations in the domain provide supplementary supervision by the physics-informed losses. To ensure a fine resolution of the three-dimensional domain, 5,000 data points and 10,000 residual points are sampled at each time step. These points are re-sampled at every epoch to provide additional coverage of the spatio-temporal domain during the training.

Motivated by the residual-based attention scheme [62] and adaptive sampling methods based on the residuals of the PDEs [50, 45], a residual-based weighting of the residual points is employed to guide the optimization of the PINNs towards regions in the domain that are challenging to optimize. In the proposed approach, the residual points are additionally weighted by a factor λ_k ranging from 0.8 to 1.2 based on the relative magnitude of the residual, calculated as

$$\lambda_i = 0.8 + 0.4 \frac{|r_i|}{\max_i(|r_i|)}, \quad (12)$$

where r_i is the residual at sampling point i .

2.3. Neural network architecture

As illustrated in Figure 1 the architecture of the PIFu neural network is adapted for the proposed PINNs. While the hourglass network for feature extraction can remain unchanged, the input and output layers, as well as the activation functions of the MLP are modified. Specifically, the MLP is comprised of 260 input nodes, with 256 nodes receiving the pixel-aligned features from the hourglass network and four nodes receiving the spatio-temporal coordinates x, y, z, t , four hidden layers with

1024, 512, 256, 128 neurons, respectively, and five output neurons for the prediction of the flow quantities ϕ, u, v, w, p . The leaky ReLu activation function [63] used as the non-linearity for the hidden layers in the MLP is replaced by the infinitely differentiable hyperbolic tangent activation function to enable the computation of higher-order derivatives through automatic differentiation. Adaptive activation functions [64] introduce an additional learnable scaling coefficient $n \cdot a$ to the activation function that regulates its slope and thus the sensibility to its inputs. The scaling coefficient consists of the fixed scale factor n and the adaptive activation coefficient a , which is optimised alongside the parameters of the neural network. Layer-wise adaptive activation functions have been found to improve the convergence rate and accuracy of PINNs across various types of problems [64], including two-phase flows [47]. Therefore, layer-wise adaptive activation functions are employed in the hidden layers with a scale factor $n = 2$ and an initial value for the adaptive activation coefficient of $a = 0.5$.

In the output layer, different activation functions are chosen for each predicted quantity according to the range of possible values. The sigmoid activation function is used for the output neuron of the phase distribution ϕ to confine the prediction within the physical bounds $\alpha \in [0, 1]$ or $C \in [-1, 1]$ for the volume fraction α in the VoF version and the order parameter C in the phase-field version of the PINNs, respectively. The prediction of the order parameter C requires an additional scaling of the activation function by a factor of two. The output neurons for the prediction of the velocity components u, v, w employ linear activation functions, while the output neuron for the prediction of the pressure p features an exponential activation function, as suggested by Buhendwa et al. [47]. Skip connections [65] are employed at each hidden layer of the MLP to propagate the information of the input feature vector and spatio-temporal coordinates to later layers in the network, which has been shown to improve the accuracy for both data-driven volumetric reconstruction [66, 34] and PINNs [67, 68].

The proposed PINNs are trained for eight epochs by the RMSPProp optimiser [69] with a learning rate decay by a factor of ten at the beginning of epochs six and eight. The batch size is reduced to 1 due to the increased computational requirements of the PINNs and the initial learning rate is accordingly decreased to 0.0001. Data augmentation through random translation of the input images is employed in order to improve the generalisation capability of the network. The augmentation of the input images by random scaling, previously used in the optimization of the data-driven reconstruction network cannot be used, as the developed PINNs are no longer scale invariant due to the surface tension term in the momentum equation, which depends on the curvature of the gas-liquid interface.

2.4. Data generation

In order to facilitate the reconstruction of the three-dimensional droplet dynamics from monocular recordings, an optical measurement technique is employed that embeds additional three-dimensional information on the three-dimensional shape of the gas-liquid interface in the images. To achieve this, the method previously proposed by the authors [70], which

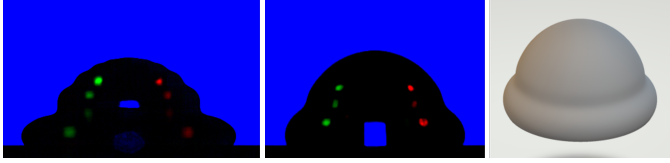


Figure 2: Recording from glare-point shadowgraphy experiment (left), synthetic image (middle) rendered from the gas-liquid interface extracted from the numerical simulation (right).

extends the canonical shadowgraphy technique by color-coded glare points from additional lateral light sources, is applied for droplet impingement experiments. In the experimental setup, a blue LED is used as the backlight for the shadowgraphy setup, which produces an accurate projection of the gas-liquid interface in the image. Additionally, two lateral red and green LED light sources are positioned at specific scattering and elevation angles relative to the droplet to produce colored glare points on the gas-liquid interface. Due to the smoothness of the phase boundary, the lateral glare points on the interface can be attributed to pure interface reflection [71]. Additional glare points arise from the two-fold refraction of the backlight as light enters and, subsequently, exits the gas-liquid interface, appearing in the central region of the droplet, as shown in Figure 2. The different colors of the glare points enable the identification of the light source, specifically the angle of incidence from each of the three light sources. Given the known geometric configuration of the light propagation, additional three-dimensional information of the gas-liquid is encoded in the position and the shape of the glare points, as previously discussed by the authors [70] and demonstrated by the successful data-driven reconstruction of the spatio-temporal interface dynamics [33]. In order to evaluate the generalisation capability of the PINNs, experiments involving the impingement of droplets on two solid substrates with different wetting properties are conducted. Specifically, the impingement of water droplets with an equivalent diameter of $d_0 = 2.27$ mm on structured Polydimethylsiloxane (PDMS) and polylactide (PLA) substrates is investigated. The surface of the PDMS substrate forms regular square grooves with a height, width, and spacing of $60 \mu\text{m}$. The surface structure further enhances the hydrophobicity of the PDMS substrate [72], which results in an equilibrium contact angle of $\theta_{eq,p} = 107^\circ$ in the parallel direction and $\theta_{eq,t} = 97^\circ$ in the transversal direction. The droplets impacted the PDMS surface at a velocity of $u_0 = 0.88$ m/s. The 3D-printed PLA substrate, produced by fused deposition modelling (FDM), features circular arc-shaped ridges with a peak-to-peak spacing of $154 \mu\text{m}$. This substrate is hydrophilic, with an equilibrium contact angle of $\theta_{eq,p} = 76^\circ$ in the parallel direction and $\theta_{eq,t} = 63^\circ$ in the transversal direction. The water droplets impacted the PLA surface at a significantly lower velocity of $u_0 = 0.45$ m/s. Experiments on both substrates were conducted at observation angles of $\omega = 0^\circ$, $\omega = 45^\circ$, and $\omega = 90^\circ$ relative to the surface structure.

Numerical simulation provides suitable ground truth data of the gas-liquid interface, as well as the velocity and pressure fields in both phases for the supervision of the network optimisation through the data loss terms. However, discrepancies arise

between the numerical simulations and the images obtained in the experiments due to differences in initial conditions, experimental uncertainties, and errors from modelling and numerical approximations. To address this matching problem, synthetic images are generated based on the gas-liquid interface geometries extracted from the numerical simulation results. For this purpose, the optical setup of the experiments is accurately reproduced in a rendering environment that allows for physically accurate ray-tracing. This enables the generation of synthetic images that not only visually match the experimental recordings but also correspond precisely to the numerical ground truth, as illustrated in Figure 2. The gas-liquid interface geometries were extracted as isosurfaces of the order parameter at $C = 0$ from three-dimensional direct numerical simulations performed by [28] within the framework of the phase-field method. These simulations involved water droplets with an equivalent diameter of $d_0 = 2.1$ mm impacting at a velocity of $u_0 = 0.62$ m/s on flat and structured hydrophobic Polydimethylsiloxane (PDMS) substrates. It is important to note that the numerical simulation and experiments both involved droplet impingement on the same PDMS substrate under similar kinematic conditions. In contrast, the experiments with the PLA substrate differed substantially from the simulation due to the substrate’s hydrophilic nature and lower kinetic energy of the droplet upon impact, leading to notably different dynamics of the gas-liquid interface. The dataset consists of 53,244 synthetic images associated with 1,479 ground truth droplet shapes. These images were generated by rotating the non-axisymmetric droplet geometries in the rendering setup in 10° increments of the observation angle ω .

2.5. Evaluation metrics

The performance of the PINNs is evaluated considering the reconstructed three-dimensional interface geometries, velocity and pressure field, as well as the availability of ground truth data. The following metrics are used for the evaluation:

- The three-dimensional intersection over union

$$3\text{D-IOU} = \frac{R \cap GT}{R \cup GT} \quad (13)$$

is calculated as the fraction of the intersection volume between the reconstructed interface R and ground truth GT and the union volume of R and GT . The 3D-IOU provides a measure for the spatial volumetric accuracy of the interface reconstruction in 3D space.

- The bias error of the reconstructed volume δ_V is calculated by the absolute deviation of the arithmetic mean

$$\bar{V} = \frac{1}{n} \sum_{i=1}^n V_{R,i} \quad (14)$$

of the reconstructed volumes V_R from the ground truth volume V_{GT} , and given relative to the ground truth volume [73]

$$\delta_V = \left| \frac{V_{GT} - \bar{V}}{V_{GT}} \right|. \quad (15)$$

- The measured uncertainty of the reconstructed volume σ_V is calculated by the standard deviation of the deviation between the reconstructed volume and the ground truth volume, and given relative to the ground truth volume [73]

$$\sigma_V = \frac{1}{V_{GT}} \sqrt{\frac{1}{n-1} \sum_{i=1}^n (V_{R,i} - \bar{V})^2}. \quad (16)$$

- The L_1 error of the predicted quantities $q \in \{u, v, w, p\}$ is calculated as

$$L_{1,q} = \frac{1}{n} \sum_{i=1}^n |q_{GT,i} - q_{pred,i}|, \quad (17)$$

over all sampling points i for one reconstructed snapshot and averaged over all samples in the the validation dataset.

- The L_2 error is calculated as

$$L_{2,q} = \sqrt{\frac{1}{n} \sum_{i=1}^n (q_{GT,i} - q_{pred,i})^2}. \quad (18)$$

The L_1 and L_2 errors are given in absolute terms or relative to the maximum $\max_i(|q_{GT,i}|)$ for a given validation sample.

3. Results and Discussion

In the following, the three proposed versions of the PINNs are first validated considering their training dynamics, with a particular focus on the convergence of the various loss terms. Afterwards, the predictive accuracy for the three-dimensional gas-liquid interface and the extended capacity for flow topology prediction are investigated by means of synthetic validation data. Finally, the results obtained by the application of the developed PINNs for the reconstruction of images recorded in the experiments are discussed. The three candidate models, *VOF-PINNs*, *PF-PINNs-v1*, and *PF-PINNs-v2* were trained on the *DFS* dataset that featured droplet impingement on flat and structured substrates and synthetically rendered images with glare points with the same set of hyperparameters, aside from the additional learnable interface thickness and chemical potential of the phase-field versions. Additionally, a purely data-driven version of the neural network is trained only on the data loss terms for validation purposes, which will be referenced as *baseline* in the following.

3.1. Validation on synthetic data

Training dynamics. The fixed weights of the data and physics-informed loss terms were iteratively tuned in order to achieve a simultaneous convergence of all loss terms, which yielded optimal training results for $w_{u,v,w,p} = 10$, $w_{Conti,adv,NS E,x} = 1000$, $w_{NSE,y} = 1$, and $w_{NSE,z} = 100$. The evolution of the various unweighted loss terms during the training of the *VOF-PINNs* for the aforementioned combination of weights are plotted in Figure 3. The other two models, *PF-PINNs-v1* and *PF-PINNs-v2*, show similar dynamics of losses during training. As can

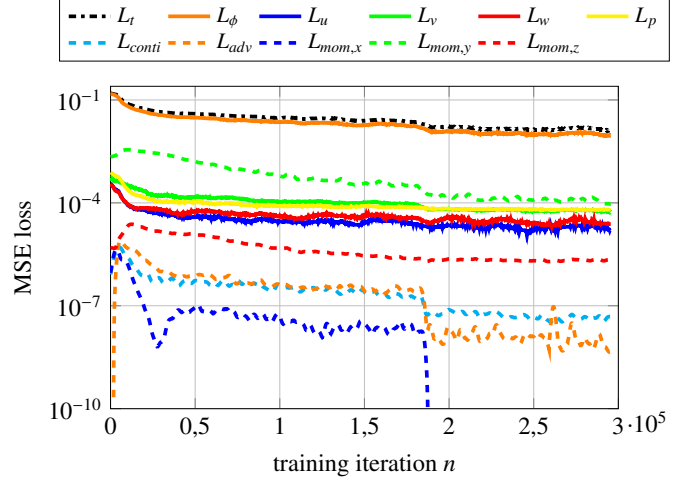


Figure 3: Evolution of the loss terms during training of the PINNs. The data loss terms are indicated by the solid lines, while the physics-informed losses are indicated by the dashed lines, and total loss is indicated by the dashed-dotted black line.

be seen, all individual loss terms are converging, which indicates the successful simultaneous learning of the phase distribution, velocities, and pressure by the neural network. The similar convergence rate of the loss terms validates the choice of loss weights. Furthermore, the difference in the magnitude of the data losses for the velocity components and pressure in comparison to the phase distribution and the even lower physics-informed loss terms highlights the necessity of loss weighting. During the initial phase of the training, the data loss for the phase distribution L_ϕ only decays slowly, which is followed by a sudden drop that can be attributed to the learning of the gas-liquid interface. A further drop can be observed at the start of epoch six, at which the first learning rate decay occurs. The first drop of L_ϕ is correlated with a sudden increase in the physics-informed loss terms. Similar training dynamics were already observed by Buhendwa et al. [47], who reported that the sudden learning of the interface location leads to a rapid increase in the magnitude of the gradients in the phase distribution at the interface and in turn, an increase in the magnitude of the surface tension term in the momentum equation. Furthermore, Buhendwa et al. [47] found that the sudden increase of the physics-informed losses destabilises the optimization and can cause complete divergence. The reason is that the physics-informed loss terms offer only limited guidance when the interface is not accurately learned and may even mislead the optimization of the neural network. This is particularly problematic for the considered water-air flow, where an erroneous prediction of the occupancy field introduces large errors in the momentum equation due to the high fluid's density ratio. In the proposed PINNs, this issue is mitigated by ensuring that the prediction of the gas-liquid interface and the flow topology has sufficiently converged before considering the physics-informed loss terms. This is successfully achieved through purely data-driven training until the loss for the phase distribution reaches the threshold value $L_{\phi,T} = 0.03$, as indicated by the monotonic decrease of all loss terms.

The gradual introduction of the data loss terms for u , v , w and p further facilitates the learning of an accurate interface prediction by focusing the optimisation on L_ϕ . The proposed loss weighting methods significantly reduced the initial plateau of the phase distribution loss, achieving faster convergence and a lower final L_ϕ . This in turn, significantly enhanced the overall training dynamics of the PINNs and has led to an increased accuracy of the prediction for the interface location, without impeding the learning of the flow topology. The second drop of L_ϕ , unlike the first, correlates with a sudden decrease of the physics-informed loss terms, which indicates that the location of the gas-liquid interface, as well as the velocity field, are learned accurately enough at this later stage of training so that further refinement of the interface location results in an improved adherence to the governing equations. Both phase-field versions of the PINNs converged to similarly low losses in comparison to the VoF version except for L_ϕ . Specifically, $PF-PINNs-v1$ with an initial value of $\epsilon_0 = 0.01$, remained at a considerably higher $L_\phi = 0.0358$ in comparison to $VOF-PINNs$ with $L_\phi = 0.0092$, while $PF-PINNs-v2$ at $\epsilon_0 = 0.01$ reached $L_\phi = 0.0135$. These results suggest that the proposed VoF approach is more appropriate for training PINNs aimed at the accurate reconstruction of the gas-liquid interface in the considered two-phase droplet flows. Furthermore, the lower L_ϕ achieved by $PF-PINNs-v2$ indicates that the separate prediction of chemical potential is beneficial for learning the phase distribution in phase-field PINNs. The cause for the better performance of $PF-PINNs-v2$ might be an improvement of the training dynamics by avoiding the fourth-order derivative in the Cahn-Hilliard equation. The learnable interface thickness of $PF-PINNs-v2$ remains close to the initial values of $\epsilon_0 = 0.01$ and $\epsilon_0 = 0.05$ throughout the training and only marginally decreases from $\epsilon = 0.01$ to $\epsilon = 0.0093$ for $PF-PINNs-v1$ towards the end of the training. It was found that a higher weighting of the interface loss term leads to lower values of ϵ , however, at the cost of significantly reduced convergence for the other loss terms, which resulted in a degraded accuracy of the interface reconstruction. Similarly, an increased initial value of ϵ_0 from 0.01 to 0.05 led to a significantly improved convergence of L_ϕ for $PF-PINNs-v2$, reaching similarly low values of $L_\phi = 0.0093$ at the end of the training in comparison to $VOF-PINNs$. Consequently, a more diffuse interface of the phase-field PINNs was found to be beneficial for their optimisation.

As the physics-informed loss terms are calculated on a different set of sampling points than the data losses, the low residuals of the governing equations indicate that a continuous and accurate function approximation in 3D space was learned by the neural network for all predicted quantities. In order to further elucidate to which extent the governing equations were learned by the PINNs, a version of the neural network was trained only through the data loss terms, while the development of the residuals was tracked during training. It was found that the PINNs achieved MSE errors for the residuals of the governing equations that were multiple orders of magnitude lower (25 to 9,600 times) in comparison to the network only trained on the data loss terms. In particular, the residuals for the interface evolution equation were reduced by almost a factor of 10^4 by the

PINNs. These results confirm the successful encoding of the underlying governing equations in the neural network by the physics-informed losses in the PINNs.

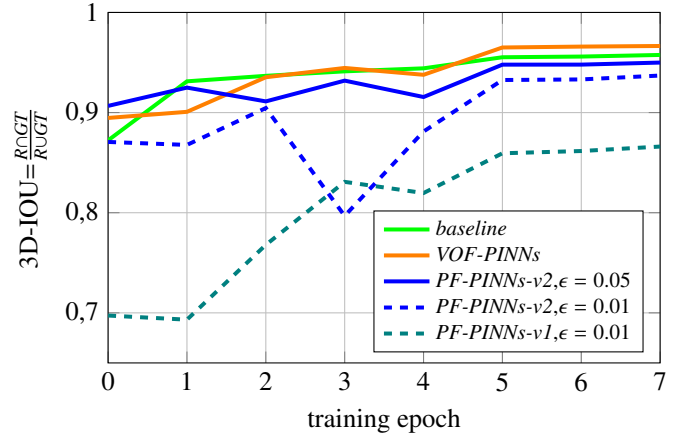


Figure 4: Average 3D-IOU of the reconstruction for the validation datasets during training of $VOF-PINNs$, as well as $PF-PINNs-v1$, and $PF-PINNs-v2$ with different capillary width ϵ_0 .

Gas-liquid interface prediction. The reconstruction accuracy of the developed PINNs is evaluated quantitatively by the results for the reconstructed gas-liquid interfaces on the synthetic validation dataset. Figure 4 shows the evolution of the 3D-IOU on the synthetic validation data during the training of the PINNs in comparison to the purely data-driven baseline network *baseline*. As can be seen, $VOF-PINNs$ reaches a higher reconstruction accuracy in comparison to *baseline*, while $PF-PINNs-v1$ and $PF-PINNs-v2$ do not yield an improvement over the data-driven baseline. More specifically, $VOF-PINNs$ reaches an accuracy of 3D-IOU=0.967, which translates to a 0.9% improvement over the data-driven baseline *baseline* with 3D-IOU=0.958, which is significant considering the proximity to optimal reconstruction results at 3D-IOU=1. By means of an ablation study for the residual-based weighting of the sampling points for the calculation of the physics-informed losses and the layer-wise adaptive activation functions, we found that both measures only marginally improved the accuracy of the interface prediction. Consequently, the gains in reconstruction accuracy can solely be attributed to the introduction of physics-informed losses to the reconstruction framework. Moreover, the different training dynamics between the VOF variant and the two phase-field versions of the PINNs are reflected in the reconstruction accuracy of the gas-liquid interface. The accuracy of $PF-PINNs-v2$ with $\epsilon_0 = 0.01$ sharply drops between training epochs two and three, which correlates to the convergence of L_ϕ below $L_{\phi,T} = 0.03$, which marks the point in training at which the physics-informed losses are introduced. A potential cause might be the onset of the identity loss for the chemical potential that couples the phase distribution to the chemical potential, which at that point in the training is still in the condition of the random initialisation. Consequently, the randomness of distribution and magnitude of the chemical potential might introduce an erroneous objective for the phase distribution through the identity loss, as

long as the prediction for the chemical potential is not yet sufficiently converged. An increase of the capillary width from $\epsilon_0 = 0.01$ to $\epsilon_0 = 0.05$ helps to mitigate this issue, leading to a substantial improvement in reconstruction accuracy, as shown in Figure 4. However, the previously observed phenomenon remains to some extent, as evidenced by the plateau in accuracy between epochs one and four. Further improvement could be reached by an additional data loss for the chemical potential, as the prediction of the chemical potential could be optimised prior to the onset of the physics-informed losses.

The impact of the different formulations of the governing equations of the VOF and phase-field PINNs on the prediction of the gas-liquid interface is further investigated by the comparison of the spatial distribution of the phases in the predictions returned by *VOF-PINNs* and *PF-PINNs-v2*. Figure 5 shows the predicted phase distribution in the in-plane and out-of-plane direction for one sample from the validation subset of the *DFS* dataset in comparison to the ground truth and the respective error distributions. The comparison of the error distributions reveals that the prediction of *PF-PINNs-v2* with $\epsilon_0 = 0.01$ features a more diffuse edge in the out-of-plane direction compared to *VOF-PINNs*, while both models predict a rather sharp in-plane phase distribution. These results indicate that the in-plane reconstruction adheres closely to the shadowgraph contour, while the out-of-plane reconstruction heavily relies on the trained model of droplet dynamics. For $\epsilon_0 = 0.05$ *PF-PINNs-v2* the out-of-plane prediction has a similar degree of diffusion compared to *VOF-PINNs*. The different diffusivity of the out-of-plane phase distribution elucidates the influence of the PINNs on the learned droplet model. A sufficiently small value for ϵ in the phase-field approach encourages the learning of a more accurately localised gas-liquid interface in comparison to the algebraic VOF approach, in which the interface thickness is not explicitly considered, but instead, a sharp interface is assumed while a certain numerical diffusion is accepted.

Velocity and pressure field prediction. The proposed PINNs provide the capability for the prediction of the three-dimensional velocity and pressure fields in both phases of the two-phase droplet flow. The accuracy of the velocity and pressure prediction by *VOF-PINNs* is evaluated on the validation dataset by the comparison to the ground truth velocity and pressure data obtained by direct numerical simulation in the phase-field method conducted by Fink et al. [28]. Figure 6 shows the predicted in-plane pressure and velocity fields in the centre plane of the droplet (left) in comparison to the ground truth (right) for one snapshot of the synthetic validation data set displayed in Figure 6a. As can be seen, there is a good topological agreement of the predicted pressure and velocity fields with the ground truth. Furthermore, the prediction of the pressure reaches a good quantitative agreement in both the in-plane and out-of-plane directions. The predicted velocity field was found to be accurately reconstructed in the liquid phase but exhibited larger deviations in the gaseous phase. Similar results were obtained for the prediction of the velocity in the out-of-plane direction, as illustrated by Appendix Figure A.13.

The results for the velocity and pressure prediction are illus-

trated in more detail in Figures 7 to 9, showing the prediction for the horizontal velocity components u and w in Figure 7, the vertical velocity component v in Figure 8 and the pressure in Figure 9 in comparison to the ground truth data and the absolute error distribution for the previous sample of the validation data. As can be seen, all three components of the predicted velocity field show an overall good topological agreement with the ground truth data. Due to the symmetry of the problem, the out-of-plane prediction for velocity component u and the in-plane prediction for w are zero, which was learned accurately by the network. As indicated by the plots of the absolute errors, the prediction of the vertical velocity component v is marginally more accurate in comparison to the horizontal velocity components, while the in-plane velocity u is predicted marginally more accurate than the out-of-plane velocity w . These results are consistent over the whole validation data set and are, furthermore, reflected in the relative L_1 and L_2 errors of the predicted quantities. The averaged relative L_1 errors for all predicted quantities lie between $L_{1,v} = 3.4$ and $L_{1,w} = 4.6\%$, while the relative L_2 errors lie between $L_{2,v} = 5.4$ and $L_{2,w} = 8.7\%$. A detailed overview of the relative and absolute errors for the prediction of the velocity and pressure distribution can be found in Appendix Tables A.1 and A.2 for the prediction by *VOF-PINNs* and *PF-PINNs-v2*, respectively. The errors for the velocity and pressure prediction by *VOF-PINNs* were consistently lower in comparison to the prediction by *PF-PINNs-v2*, which indicates that the proposed VOF approach, in addition to a more accurate prediction of the interface, also allows a better prediction of the velocity and pressure. The relative errors of all predicted quantities varied across the validation dataset, which follows the dynamic deformation of the droplet and exhibits decaying values for velocity and pressure due to the damped oscillation of the interface. No substantial outliers or clear trend were observed for the development of the errors, in contrast to the observation of Qiu et al. [49], who found that low absolute velocities correlated with high relative errors, due to the focus of the optimisation on training samples with large velocities. These results indicate that the proposed PINNs successfully learned to predict the velocity and pressure consistently during the dynamic deformation of the droplet. A potential reason for the more consistent results might be the employed training dataset, which consists mostly of samples with low velocities due to the aforementioned nature of droplet impingement, which in turn could balance out the influence of the relatively high losses from high-velocity samples. The evolution of the relative and absolute errors for *VOF-PINNs* on the subset of the validation data that features droplet impingement on a structured surface are plotted in Appendix Figures A.14 and A.15, respectively.

The comparison of the in-plane and the out-of-plane predictions reveals a higher in-plane accuracy for all predicted quantities. While comprehensive image features from the shadowgraphy contour are available for the in-plane prediction, the out-of-plane prediction depends on the trained model of the droplet dynamics and the 3D information encoded in the glare points. However, in comparison to the prediction of the gas-liquid interface, the available information for the velocity and pressure reconstruction is even more limited. Only the temporal evolu-

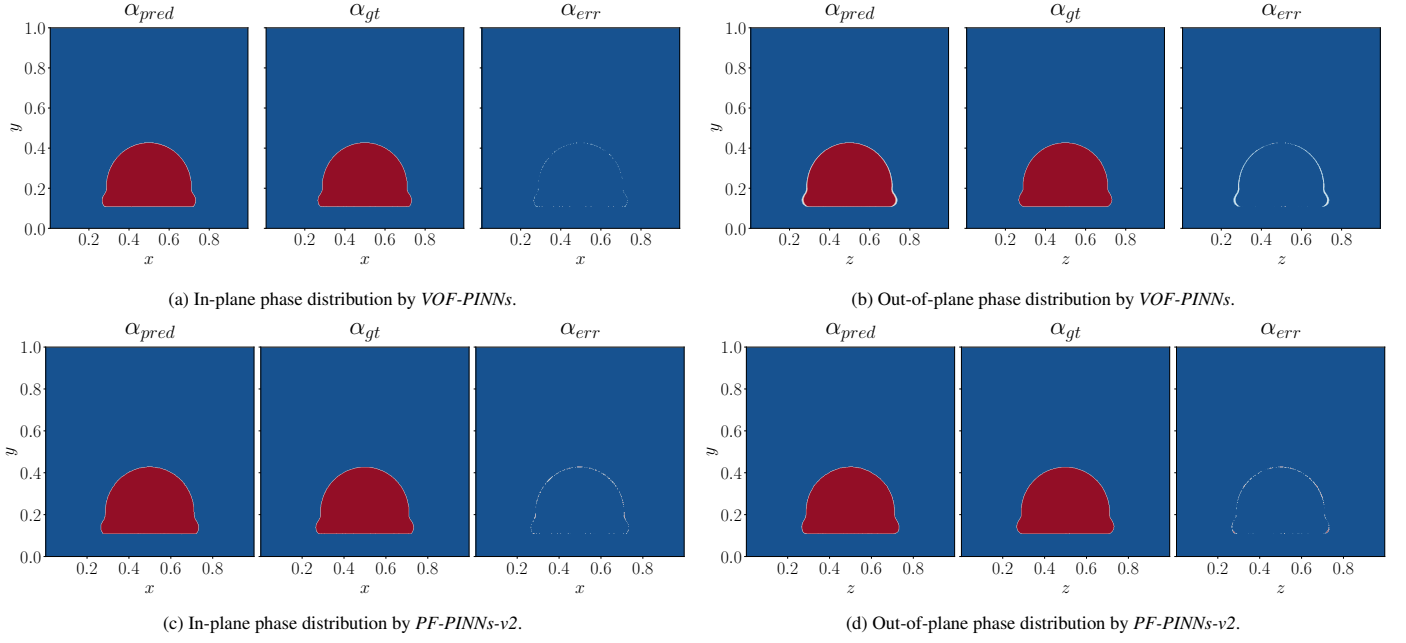
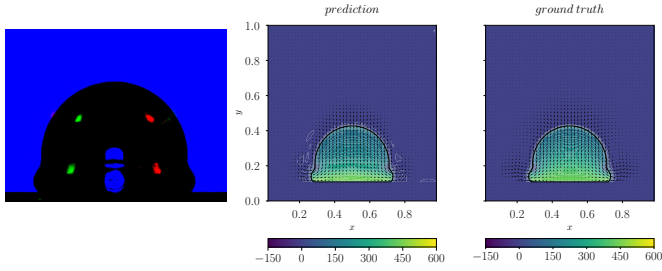


Figure 5: Phase distribution predicted by *VOF-PINNs* (top) and *PF-PINNs-v2* with $\epsilon_0 = 0.01$ (bottom) along the centre planes of the droplet in the in-plane and out-of-plane directions (left) in comparison to the ground truth simulation data (middle) and the absolute error between the prediction and the ground truth (right).



(a) Synthetic input image (b) Predicted velocity vector field and pressure contours in rendered from a simulated [Pa] along the centre plane of the droplet (left) in comparison to the ground truth simulation data (right). The contour of the gas-liquid interface is indicated by the black solid line.

Figure 6: Snapshot from the validation data set (a) and respective in-plane reconstruction (b) by *VOF-PINNs*.

tion of the interface contour and the glare points provide some cues for the reconstruction, as the bulk of the shadowgraph does not carry any information for the velocity and pressure, as opposed to the phase distribution. Consequently, only the in-plane velocity at the contour and the glare points can be predicted with the support of image features, while the rest of the flow topology and pressure distribution have to be inferred from the trained model of droplet dynamics. The capability of the proposed PINNs to infer the three-dimensional distribution of these hidden quantities from the limited information in the input images demonstrates the capability of the physics-informed learning approach.

As observed in Figures 7 and 8 the accuracy of the velocity prediction inside of the droplet is higher in comparison to the outside. A likely cause for this difference is the signifi-

cantly greater contribution of the physics-informed losses for the momentum equation in the liquid phase in comparison to the gaseous phase, due to the higher density and viscosity, which leads to higher residuals in the liquid phase and, thereby, focuses the optimisation of the physics-informed losses on the inside of the droplet. Another source of prediction discrepancies in the outer region, farther from the interface, might arise from the outer boundary condition applied in the simulation (zero-gradient for velocity), which was intentionally omitted in the PINN implementation. This omission is deliberate, aiming to better capture arbitrary realistic distributions observed at the boundaries in experimental shadowgraphs. Furthermore, the errors in the vicinity of the gas-liquid interface are significantly lower compared to the rest of the domain, which is most obvious for the prediction of the pressure distribution (see Figure 9). These results are likely related to the local refinement of the sampling points at the interface and the residual-based weighting. The higher density of the sampling points for both the data and physics-informed loss calculation focuses the optimisation on the interface, while the residual-based weighting further reinforces the physics-informed losses at the interface. As can be seen most saliently in Figure 8(a) the prediction by the PINNs completes the velocity field in a physically reasonable manner, which indicates a certain capability for the extrapolation of prediction outside of the training data domain.

The successful prediction of the three-dimensional flow topology in combination with an improvement in the accuracy of the gas-liquid interface reconstruction on the synthetic data validates the proposed approach based on PINNs. The optimisation of the phase distribution and velocity field is mutually dependent, as they are coupled by physics-informed loss derived from the residuals of the interface evolution equation. Thereby,

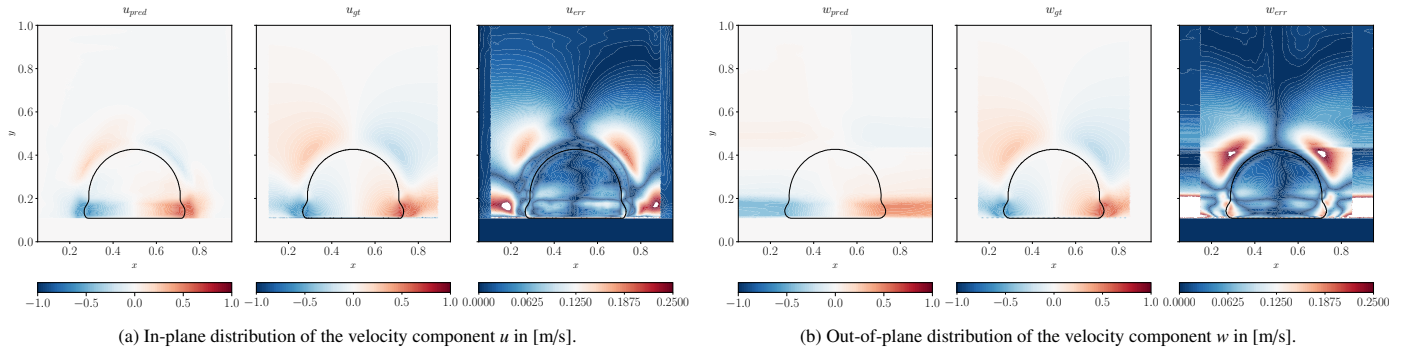


Figure 7: Prediction of *VOF-PINNs* for the horizontal components of the velocity vector along the centre planes of the droplet in the in-plane and out-of-plane directions (left) in comparison to the ground truth simulation data (middle) and the absolute error between the prediction and the ground truth (right).

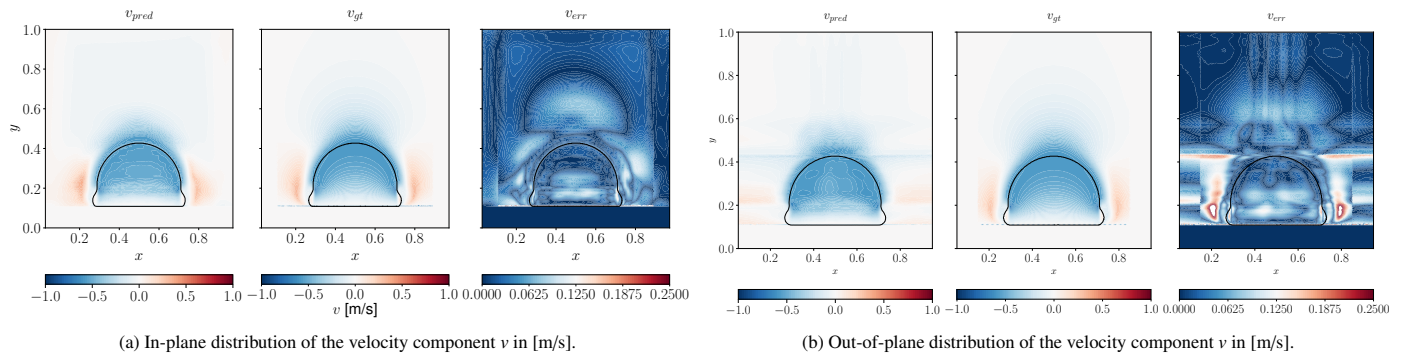


Figure 8: Prediction of *VOF-PINNs* for the vertical component of the velocity vector along the centre planes of the droplet in the in-plane and out-of-plane directions (left) in comparison to the ground truth simulation data (middle) and the absolute error between the prediction and the ground truth (right).

the learning of an accurate velocity distribution at the interface promotes the learning of the interface location and vice versa. The accurate prediction for both the phase distribution and the velocity field in combination with low residuals for the interface evolution equation at the end of the training indicates that the underlying physics were successfully encoded in the neural network during the optimisation of the PINNs. The developed PINNs were optimized towards a high accuracy of the gas-liquid interface, which supports an improvement of the velocity and pressure prediction by a different weighting of the loss terms during optimisation.

3.2. Reconstruction of experimental data

We now employ the PINNs that were trained and validated on the synthetic data for the reconstruction of images recorded in the experiments by means of the glare-point shadowgraphy technique in order to evaluate their effectiveness in real-world applications. The same experimental data of droplet impingement on structured PLA and PDMS substrates is used for the evaluation of the baseline data-driven reconstruction technique to allow for a quantitative comparison of the reconstruction performance of both approaches. The following evaluation focuses on the VOF version of the developed PINNs, *VOF-PINNs*, which achieved superior performance among the three candidate models on the synthetic validation data.

Gas-liquid interface reconstruction. Overall, we found a substantial improvement of the reconstruction accuracy by the pro-

posed PINNs in comparison to the data-driven baseline *baseline* for the prediction of the gas-liquid interface on experimental data. The visual inspection of the reconstruction results for experiments with both substrates at different observation angles reveals that the gas-liquid interfaces reconstructed by the PINNs are smoother and more consistent over time in comparison to the reconstruction of *baseline*. A comparison of the reconstruction results obtained by *baseline* and *VOF-PINNs* is shown in Figure 10. The curvature of the interface reconstruction by *VOF-PINNs* appears to be more physical, as small-scale features with a high curvature that can be observed for the purely data-driven reconstruction are not present in the reconstruction by the PINNs. At the considered *We*-number, such features are unphysical, as the surface tension of the gas-liquid interface counteracts the formation of high curvatures. These results indicate that the consideration of surface tension in the momentum equation of the PINNs had a positive regularising effect on the optimisation of the neural network that led to a more physical reconstruction of the gas-liquid interface. Furthermore, the temporal evolution of the gas-liquid interface appears to be smoother for the reconstruction of the PINNs in comparison to the data-driven baseline, as the volume of the droplet remains more stable in time, unlike the fluctuation of the volume observed in the purely data-driven reconstruction.

These results are illustrated in Figure 11, which shows the temporal evolution of the normalised integral droplet volume for the reconstruction of *VOF-PINNs* and *baseline* for exper-

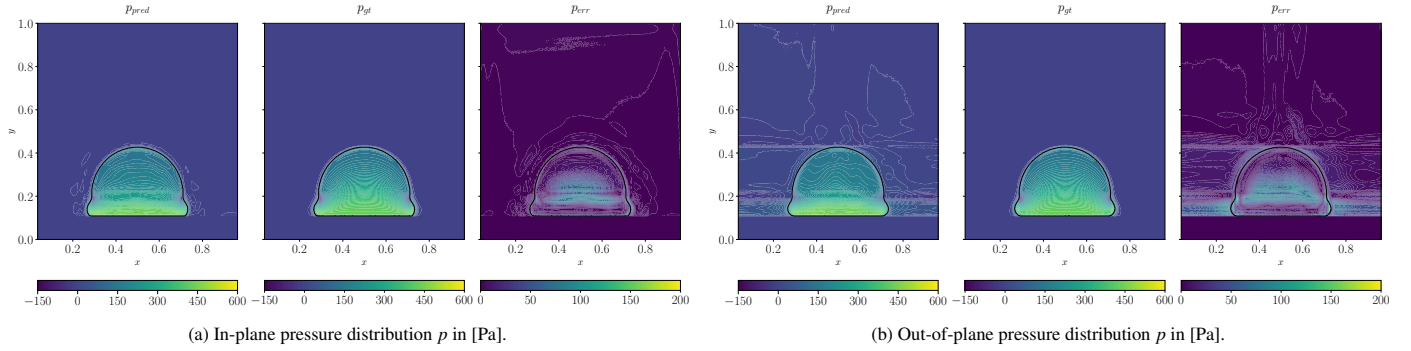


Figure 9: Prediction of *VOF-PINNs* for the pressure distribution along the centre planes of the droplet in the in-plane and out-of-plane directions (left) in comparison to the ground truth simulation data (middle) and the absolute error between the prediction and the ground truth (right). The predicted contour of the droplet gas-liquid interface is indicated by the black solid line overlaid on the prediction and analogously the ground truth contour is overlaid on the ground truth velocity and pressure distributions.

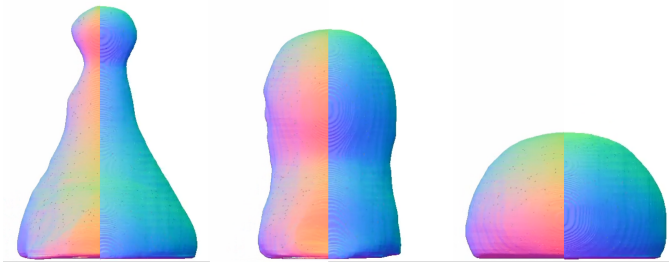


Figure 10: Out-of-plane reconstruction by *baseline* (left half) and *VOF-PINNs* (right half) for three different recordings from the experiments involving droplet impingement on the structured PDMS substrate at an observation angle of $\omega = 45^\circ$. The droplet geometry reconstructed by *VOF-PINNs* is mirrored vertically to allow for a direct comparison of the reconstructed contours.

iments that featured droplet impingement on the structured PDMS substrate at an observation angle of $\omega = 90^\circ$. Throughout the entire period of time, the reconstruction of the PINNs lies significantly closer to the ground truth volume, indicated by the black line and hence remains more conservative. Both reconstruction techniques exhibit larger errors immediately after the impingement of the droplet, which correlates with the strongest droplet deformation. However, the maximum error is significantly reduced by *VOF-PINNs* as compared to *baseline*. Furthermore, the prediction of *baseline* underestimates the volume of the droplet on average, while the average prediction of *VOF-PINNs* is close to the ground truth volume. Consequently, *VOF-PINNs* achieves a significantly lower uncertainty and bias error of the reconstructed volume of the droplet in comparison to *baseline*. Specifically, *VOF-PINNs* reaches an average uncertainty of $\sigma_V = 2.0\%$ and bias error of $\delta_V = 2.2\%$ in comparison to $\sigma_V = 6.2\%$ and bias error of $\delta_V = 5.7\%$ by *baseline*, effectively reducing the errors by a factor of three. It should be noted, that while a dedicated effort was made to ensure a fair comparison of the PINNs with the data-driven baseline model, both approaches require a different optimisation, including tuning of hyperparameters and weighting of the loss terms. Consequently, the optimisation of both networks and, in turn, their reconstruction performance could still be further improved, thus changing the comparison of the performance.

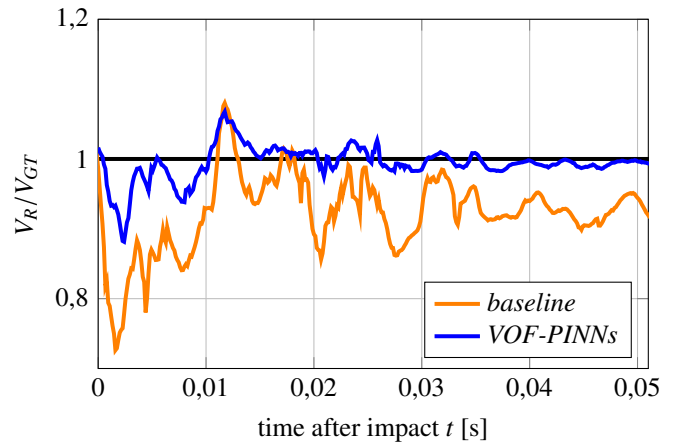


Figure 11: Temporal evolution of the normalised integral volume of the reconstruction for droplet impingement on the structured PDMS-substrate at $\omega = 90^\circ$ observation angle with *VOF-PINNs* and *baseline*.

It should be noted, that a second version of the baseline data-driven model was trained with the same set of hyperparameters as the PINNs for a direct comparison, which yielded very similar results to *baseline*. The substantial improvement of the reconstruction accuracy of the gas-liquid interface by the PINNs, however, suggests that the introduction of further prior knowledge through the physical constraints during training is an effective measure to enhance the trained model of the droplet dynamics. The lower errors by the PINNs in comparison to the data-driven baseline are consistently achieved for the reconstruction of all considered experiments, involving the impingement of droplets on structured PLA and PDMS substrates at different observation angles, as detailed in Appendix Table A.3. This includes varying degrees of gas-liquid interface deformation, as the impingement on the hydrophobic PDMS substrate leads to noticeably greater deformation of the droplet, demonstrating that the developed PINNs are adaptable towards different experimental conditions. Consequently, the developed PINNs, which were trained on two cases of numerical simulation, are able to generalise to different fluid mechanical conditions. Furthermore, the enhancement of the predictive accuracy for the

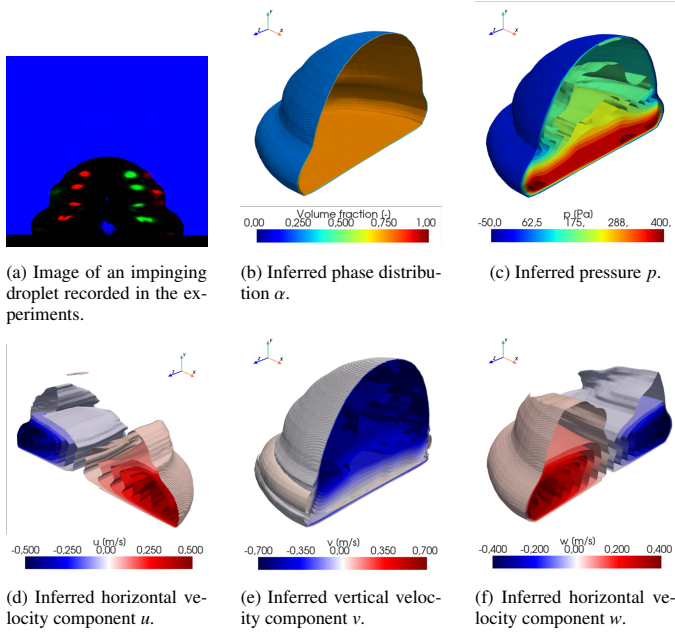


Figure 12: Snapshot from the experiment involving droplet impingement on the structured PLA substrate (a) and iso-contours of the prediction by *VOF-PINNs*, phase distribution α indicating the gas-liquid interface (b), pressure p (c), horizontal velocity component u (d), vertical velocity component v (e), horizontal velocity component w (f).

gas-liquid interface that was observed for the reconstruction of the synthetic validation data carried over well to the prediction of experiments, which indicates that the approach of training on synthetic data is suitable for the proposed PINNs.

Velocity and pressure reconstruction. Figure 12 shows the inferred velocity and pressure distribution by *VOF-PINNs* for one snapshot of the experiments involving droplet impingement on the structured PLA substrate. As can be seen, the PINNs are able to infer the continuous three-dimensional flow field inside of the droplet from a single input image. The comparison to snapshots at similar time instances and with comparable droplet geometries in the numerical simulation reveals that for some samples the velocity and pressure were inferred in a physically reasonable manner, while other frames yielded unphysical results. In particular, the velocity prediction failed at time instances that coincide with the inflection points of the droplet’s motion at which the acceleration of the gas-liquid interface approached zero and the velocity changed sign. Notably, the first of these inflection points, which occurred during the transition from the spreading phase to the retraction phase (see Rioboo et al. [74, 75] for further details), was correctly predicted by the PINNs. However, the second inflection point at the end of the retraction phase and the transition to the second spreading phase resulted in a high uncertainty of the velocity prediction, indicated by large fluctuations of the predicted velocity field. This behaviour repeated at the following inflection points. Furthermore, the deformation of the droplet led to a self-occlusion of the gas-liquid interface in the input image, which resulted in increased errors in the velocity prediction. In contrast, the pressure prediction remained physically reasonable and similar

to the validation data of the numerical simulation throughout the dynamic deformation of the droplet. In particular, the elevated dynamic pressure close to liquid-solid contact upon impact and the negative Laplace pressure at the negatively curved regions of the interface (cmp. Figure 12f) were successfully reconstructed for different experimental conditions. While the inference of the velocity and pressure yielded accurate results for the synthetic validation data, these results could only partly be reproduced on the real data distribution, which involved different experimental conditions and, thereby, different droplet geometries in comparison to the training data. Consequently, the ability for the prediction of the velocity and pressure did not generalise as well as the prediction of the gas-liquid interface. This issue is likely related to the scarcity of information available for the velocity and pressure prediction. These results further substantiate the hypothesis that the predictive capability for the phase distribution generalises well to novel droplet geometries due to the extracted image features, which provide additional information on the gas-liquid interface, but only indirectly for the velocity and pressure. The inference of the velocity and pressure thus relies more on the trained model of droplet dynamics. Consequently, the addition of further information in the images related to these quantities would likely improve the generalisation capability towards different experimental conditions. Furthermore, the optimisation of the PINNs was focused on the accurate prediction of the gas-liquid interface by a specific weighting of the loss terms. Therefore, improved results for the prediction of the velocity and pressure distributions can be expected for an increased relative weighting of the velocity and pressure data loss terms.

4. Summary

The presented results for the accurate three-dimensional reconstruction of the two-phase flow dynamics from planar measurement data, exemplified for an impinging droplet, demonstrate the success of the proposed approach based on convolutional feature extraction and physics-informed neural networks (PINNs). The integration of localized spatially aligned features extracted by a convolutional hourglass network allows the developed PINNs to effectively leverage the volumetric information encoded in the images recorded through the purposefully developed glare-point shadowgraphy technique. The convolutional features provide a robust and information-rich foundation for the reconstruction, which facilitates significant generalisation capabilities, demonstrated by the accurate reconstruction of experiments with varying fluid mechanical conditions in comparison to the synthetic training data. In particular, the in-plane reconstruction generalizes well to unfamiliar interface shapes because the shadowgraphy contours provide a reliable and spatially accurate information of the planar gas-liquid interface location. For out-of-plane reconstruction, the approach relies more on the encoded droplet dynamics within the PINNs, supplemented by the additional information of the three-dimensional gas-liquid interface encoded in the glare points, which allows for an accurate depth estimation. The

successful reconstruction of three-dimensional gas-liquid interface dynamics from real measurement data indicates that synthetic training data can effectively prepare PINNs for accurate experimental applications. To the best of the author’s knowledge, the present work marks the first application of PINNs to real measurement data of two-phase flows, demonstrating the feasibility of the approach. Remarkably, even a limited training dataset, consisting of only two numerical simulation cases, proved sufficient for training the PINNs. The incorporation of the governing equations of two-phase flows through physics-informed losses derived from the Navier-Stokes, continuity, and interface evolution equations, results in a smoother, more physically accurate interface reconstruction compared to the data-driven baseline, demonstrating the successful learning of two-phase flow dynamics by the PINNs. Furthermore, the temporal consistency of the reconstruction was significantly improved, resulting in better conservation of the droplet’s volume over time and a notable reduction in uncertainty.

The challenge of learning the sharp interfaces in two-phase flows by means of PINNs was successfully addressed by the local refinement of sampling points around the interface. Prioritizing the learning of the phase distribution was found to be crucial, as the high density ratio of the considered water-air flows necessitates precise phase information for accurate physics-informed losses of the momentum equation. This was achieved by first pre-training the network on data to accurately capture the phase distribution, followed by the learning of velocity and pressure, and finally incorporating the physics-informed losses. The physics-informed loss of the interface evolution equation, couple the learning of the gas-liquid interface location and the velocity distribution at the interface. The accurate reconstruction of the interface location and the velocity field around the gas-liquid for the synthetic validation data in combination with low residuals of the interface evolution equation reveals that this relationship was learned well by the PINNs. The simplicity of the VOF approach in combination with a superior accuracy of the predicted phase distribution and interface location in comparison to the phase-field approach renders it more suitable for the considered two-phase droplet flows. However, the explicit modelling of interface thickness in the phase-field approach enables the learning of thin interfaces, which may be valuable for certain applications. The control of interface thickness was identified as an important parameter for optimizing phase-field PINNs. Additionally, predicting the chemical potential separately in phase-field PINNs significantly improved neural network optimization and predictive accuracy, while reducing computational demands by avoiding the calculation of fourth-order derivatives in the Cahn-Hilliard equations, leading to faster training with fewer computational resources.

The developed PINNs offer prospects for the prediction of continuous three-dimensional velocity and pressure fields for both phases. The accurate quantitative prediction of velocity and pressure distributions on synthetic data, along with the promising reconstruction results for the flow topology on real measurement data, demonstrate that the inference of these hidden quantities from optical experiments using PINNs is feasible, though further development is needed to ensure reliable

results. Since the proposed PINNs were optimised for the accurate prediction of the gas-liquid interface, adjusting the loss weighting could improve velocity and pressure learning. Additionally, incorporating more measurement data for the velocity or pressure could be beneficial for enhancing the accuracy of these predictions. The direct processing of images obtained by particle image velocimetry by the proposed convolutional-feature enhanced PINNs appears likewise feasible and promising. A further improvement of the reconstruction accuracy can potentially be achieved by feature expansion techniques, such as Fourier feature mapping [76], which has been shown to mitigate the spectral bias of neural networks towards lower frequencies and, thus, might facilitate the learning of a sharp gas-liquid interface. This approach has recently been applied successfully for the learning of 3D representations [76] and PINNs [77].

The developed convolutional feature-enhanced PINNs seamlessly integrate prior knowledge from numerical simulations and the governing equations of two-phase flows with observations from glare point shadowgraphy experiments. This regularization enables the reconstruction of 3D spatio-temporal droplet dynamics from a single slice of 2D measurement data. The presented approach offers a versatile framework for the post-processing of two-phase flow experiments, as the accurate measurement of the interface position can be easily obtained by the glare-point shadowgraphy technique across various two-phase flows. The application to droplets in fuel cells, spays, or bubble flows appears straightforward, while an extension to other physical problems that can be captured with optical measurement techniques appears feasible.

5. Acknowledgements

This work was performed on the HoreKa supercomputer funded by the Ministry of Science, Research and the Arts Baden-Württemberg and by the Federal Ministry of Education and Research. We gratefully acknowledge the financial support from the Karlsruhe House of Young Scientists (KHYS), which contributed to funding the research visit of Maximilian Dreisbach to the Crunch Group led by Prof. George Em Karniadakis that initiated the collaboration in this work. E.K and G.E.K would like to acknowledge the support from the AIM for Composites, an Energy Frontier Research Center funded by the U.S. Department of Energy (DOE), Office of Science, Basic Energy Sciences (BES) under Award #DE-SC0023389 as well as MURI/ONR project.

Appendix A. Appendix

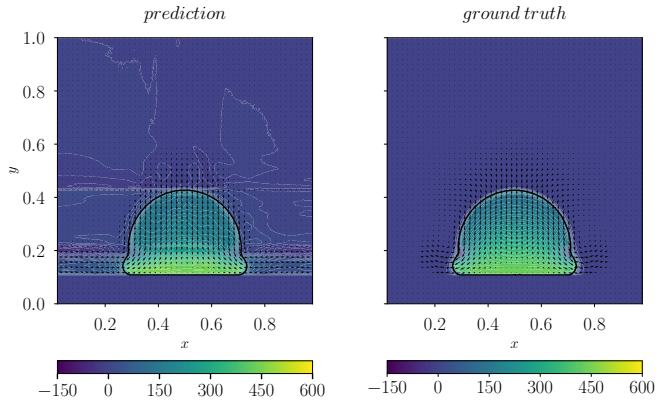


Figure A.13: Predicted velocity vector field and pressure contours along the centre plane of the droplet (left) in comparison to the ground truth simulation data (right). The contour of the gas-liquid interface is indicated by the black solid line.

Table A.1: Absolute and relative L_1 , L_2 errors of the predicted flow quantities u , v , w and p by *VOF-PINNs*.

quantity	abs. L_1	abs. L_2	rel. L_1	rel. L_2
u [m/s]/[%]	0.0187	0.0500	3.44	7.43
v [m/s]/[%]	0.0229	0.0403	3.26	5.43
w [m/s]/[%]	0.0240	0.0539	4.64	8.71
p [Pa]/[%]	12.81	19.179	4.58	6.77

Table A.2: Absolute and relative L_1 , L_2 errors of the predicted flow quantities u , v , w and p by *PF-PINNs-v2*.

quantity	abs. L_1	abs. L_2	rel. L_1	rel. L_2
u [m/s]/[%]	0.0242	0.0548	5.0	9.19
v [m/s]/[%]	0.0344	0.0511	5.01	7.15
w [m/s]/[%]	0.0376	0.0711	7.53	12.39
p [Pa]/[%]	20.095	27.700	7.48	10.12

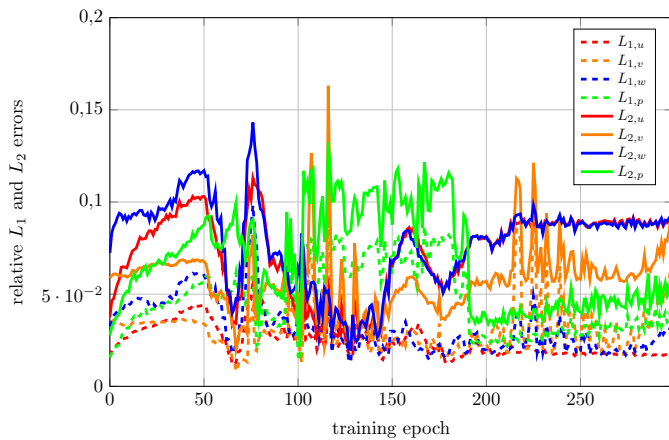


Figure A.14: Relative L_1 (dashed lines) and L_2 (solid lines) errors of velocity and pressure fields.

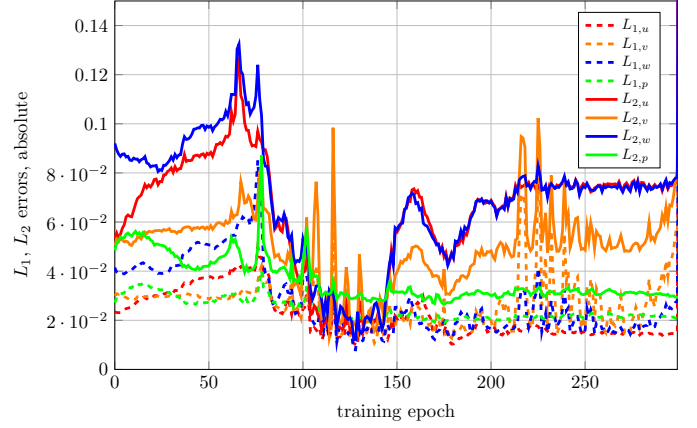


Figure A.15: Absolute L_1 (dashed lines) and L_2 (solid lines) errors of velocity and pressure fields.

Table A.3: Uncertainty σ_V and bias error δ_V of the reconstructed integral volume for *baseline* and *VOF-PINNs* in percent of ground truth volume for droplet impingement on different substrates.

case	<i>baseline</i>		<i>VOF-PINNs</i>	
	σ_V	δ_V	σ_V	δ_V
PLA 0°	8.2	9.1	2.3	5.1
PLA 45°	3.5	0.7	1.4	1.1
PLA 90°	8.2	5.4	2.2	0.2
PDMS 0°	9.4	5.6	3.3	3.0
PDMS 45°	2.9	5.1	1.3	3.7
PDMS 90°	3.9	6.1	1.8	0.01

References

- [1] A.L.N. Moreira and Miguel Panão. Spray-wall impact. In *Handbook of Atomization and Sprays: Theory and Applications*, pages 441–455. Springer, Heidelberg, 2011.
- [2] R. Andrade, O. Skurtys, and F. Osorio. Drop impact behavior on food using spray coating: Fundamentals and applications. *Food Research International*, 54:397–405, 2013.
- [3] Alireza Dalili, Sanjeev Chandra, Javad Mostaghimi, H.T. Charles Fan, and Joseph C. Simmer. Bubble entrapment and escape from sprayed paint films. *Progress in Organic Coatings*, pages 153–165, 2016.
- [4] Detlef Lohse. Fundamental fluid dynamics challenges in inkjet printing. *Annu. Rev. Fluid Mech.*, 54:349–382, 2022.
- [5] V. Thoreau, B. Malki, G. Berthome, L. Boulange-Petermann, and J. C. Joud. Physico-chemical and dynamic study of oil-drop removal from bare and coated stainless-steel surfaces. *Journal of Adhesion Science and Technology*, 20(16):1819–1831, 2006. ISSN 0169-4243. doi: 10.1163/156856106779116669.
- [6] G. K. Seevaratnam, H. Ding, O. Michel, J.Y.Y. Heng, and O. K. Matar. Laminar flow deformation of a droplet adhering to a wall in a channel. *Chemical Engineering Science*, 65(16):4523–4534, 2010. ISSN 0009-2509. doi: 10.1016/j.ces.2010.04.012. URL <https://www.sciencedirect.com/science/article/pii/S0009250910002514>.
- [7] L. Thompson. The role of oil detachment mechanisms in determining optimum detergency conditions. *Journal of Colloid and Interface Science*, 163(1):61–73, 1994. ISSN 0021-9797. doi: 10.1006/jcis.1994.1080. URL <https://www.sciencedirect.com/science/article/pii/S0021979784710800>.
- [8] Anthony D. Schleizer and Roger T. Bonnecaze. Displacement of a two-dimensional immiscible droplet adhering to a wall in shear and pressure-driven flows. *Journal of Fluid Mechanics*, pages 29–54, 1999. ISSN 0022-1120. doi: 10.1017/S0022112098003462.
- [9] A. K. Gupta and S. Basu. Deformation of an oil droplet on a solid substrate in simple shear flow. *Chemical Engineering Science*, 63(22):5496–5502, 2008. ISSN 0009-2509. doi: 10.1016/j.ces.2008.07.027. URL <https://www.sciencedirect.com/science/article/pii/S0009250908004119>.
- [10] S. Madani and A. Amirfazli. Oil drop shedding from solid substrates by a shearing liquid. *Colloids and Surfaces A: Physicochemical and Engineering Aspects*, 441:796–806, 2014. ISSN 09277757. doi: 10.1016/j.colsurfa.2013.04.058. URL <https://www.sciencedirect.com/science/article/pii/S0927775713003701>.
- [11] C. Korte and A. M. Jacobi. Condensate retention effects on the performance of plain-fin-and-tube heat exchangers: Retention data and modeling. *Journal of Heat Transfer*, 123(5):926–936, 2001. ISSN 0022-1481. doi: 10.1115/1.1391276.
- [12] Satish G. Kandlikar and Mark E. Steinke. Contact angles and interface behavior during rapid evaporation of liquid on a heated surface. *International Journal of Heat and Mass Transfer*, 45(18):3771–3780, 2002. doi: 10.1016/S0017-9310(02)00090-X. URL <https://www.sciencedirect.com/science/article/pii/S001793100200090X>.
- [13] Linn Karlsson, Henrik Lycksam, Anna-Lena Ljung, Per Gren, and T. Staffan Lundström. Experimental study of the internal flow in freezing water droplets on a cold surface. *Experiments in Fluids*, 60(12):182, 2019. ISSN 0723-4864. doi: 10.1007/s00348-019-2823-1.
- [14] A. Theodorakakos, T. Ous, M. Gavaises, J. M. Nouri, N. Nikolopoulos, and H. Yanagihara. Dynamics of water droplets detached from porous surfaces of relevance to pem fuel cells. *Journal of Colloid and Interface Science*, 300(2):673–687, 2006. ISSN 0021-9797. doi: 10.1016/j.jcis.2006.04.021.
- [15] E. C. Kumbur, K. V. Sharp, and M. M. Mench. Liquid droplet behavior and instability in a polymer electrolyte fuel cell flow channel. *Journal of Power Sources*, 161(1):333–345, 2006. ISSN 0378-7753. doi: 10.1016/j.jpowsour.2006.04.093. URL <https://www.sciencedirect.com/science/article/pii/S037877530600663X>.
- [16] Angelo Esposito, Aaron D. Montello, Yann G. Guezennec, and Cesare Pianese. Experimental investigation of water droplet–air flow interaction in a non-reacting pem fuel cell channel. *Journal of Power Sources*, 195(9):2691–2699, 2010. ISSN 0378-7753. doi: 10.1016/j.jpowsour.2009.11.078. URL <https://www.sciencedirect.com/science/article/pii/S0378775309020862>.
- [17] Sebastian Burgmann, Mirja Blank, Ulla Panchenko, and Jens Wartmann. μ piv measurements of two-phase flows of an operated direct methanol fuel cell. *Experiments in Fluids*, 2013. doi: 10.1007/s00348-013-1513-7.
- [18] Yucheng Fu and Yang Liu. 3D bubble reconstruction using multiple cameras and space carving method. *Measurement Science and Technology*, page 075206, 2018.
- [19] Ashik Ullah Mohammad Masuk, Ashwanth Salibindla, and Rui Ni. A robust virtual-camera 3D shape reconstruction of deforming bubbles/droplets with additional physical constraints. *International Journal of Multiphase Flow*, page 103088, 2019.
- [20] H. Erbil, Glen McHale, and Michael Newton. Drop evaporation on solid surfaces: Constant contact angle mode. *Langmuir : the ACS journal of surfaces and colloids*, 18, 2002. doi: 10.1021/la011470p.
- [21] S. M. Rowan, G. McHale, M. I. Newton, and M. Toorneman. Evaporation of microdroplets of three alcohols. *The Journal of Physical Chemistry B*, 101(8):1265–1267, 1997. ISSN 1520-6106. doi: 10.1021/jp962795v.
- [22] G. Minor, N. Djilali, D. Sinton, and P. Oshkai. Flow within a water droplet subjected to an air stream in a hydrophobic microchannel. *Fluid Dynamics Research*, 41(4):045506, 2009. ISSN 0169-5983. doi: 10.1088/0169-5983/41/4/045506.
- [23] Sebastian Burgmann, Michael Dues, Beawer Barwari, Jonas Steinbock, Lars Büttner, Jürgen Czarske, and Uwe Janoske. Flow measurements in the wake of an adhering and oscillating droplet using laser-doppler velocity profile sensor. *Experiments in Fluids*, page 47, 2021.
- [24] Haruyuki Kinoshita, Shohei Kaneda, Teruo Fujii, and Marie Oshima. Three-dimensional measurement and visualization of internal flow of a moving droplet using confocal micro-piv. *Lab on a chip*, 7(3):338–346, 2007. ISSN 1473-0197. doi: 10.1039/B617391H.
- [25] M. Duxenneuner, Oliver Pust, Peter Fischer, Erich Windhab, and Justin Cooper-White. *Flow visualization of a forming droplet in a micro channel with FlexPIV*. 2009.
- [26] Kwan Hyoung Kang, Sang Joon Lee, Choung Mook Lee, and In Seok Kang. Quantitative visualization of flow inside an evaporating droplet using the ray tracing method. *Measurement Science and Technology*, 15(6):1104, 2004. ISSN 0957-0233. doi: 10.1088/0957-0233/15/6/009.
- [27] G. Minor, Peter Oshkai, and Ned Djilali. Optical distortion correction for liquid droplet visualization using the ray tracing method: Further considerations. *Measurement Science and Technology*, 18:L23, 2007. ISSN 0957-0233. doi: 10.1088/0957-0233/18/11/L01.
- [28] V. Fink, X. Cai, A. Stroh, R. Bernard, J. Kriegseis, B. Frohnapfel, H. Marschall, and M. Wörner. Drop bouncing by micro-grooves. *International Journal of Heat and Fluid Flow*, 70:271–278, 2018.
- [29] M. Wörner, N. Samkhaniani, X. Cai, Y. Wu, A. Majumdar, H. Marschall, B. Frohnapfel, and O. Deutschmann. Spreading and rebound dynamics of sub-millimetre urea-water-solution droplets impinging on substrates of varying wettability. *Applied Mathematical Modelling*, pages 53–73, 2021.
- [30] Veronika Krämer, Beawer Barwari, Sebastian Burgmann, Martin Rohde, Simon Rentschler, Christopher Holzknacht, Christoph Gmelin, and Uwe Janoske. Numerical analysis of an adhering droplet applying an adapted feedback deceleration technique. *International Journal of Multiphase Flow*, page 103808, 2021.
- [31] S.F. Kistler. Hydrodynamics of wetting. In J.C. Berg, editor, *Wettability*, pages 311–430. Marcel Dekker, New York, 1993.
- [32] R. Cox. The dynamics of the spreading of liquids on a solid surface. part 1. viscous flow. *J. Fluid Mech.*, pages 169–194, 1986.
- [33] Maximilian Dreisbach, Jochen Kriegseis, and Alexander Stroh. Spatio-temporal reconstruction of drop impact dynamics by means of color-coded glare points and deep learning. *Measurement Science and Technology*, 2024. doi: 10.1007/s00348-023-03592-0.
- [34] S. Saito, Z. Huang, R. Natsume, S. Morishima, A. Kanazawa, and H. Li. PIFu: pixel-aligned implicit function for high-resolution clothed human digitization. In *Proceedings of the IEEE/CVF International Conference on Computer Vision (ICCV)*, 2019.
- [35] M. Raissi, P. Perdikaris, and G. E. Karniadakis. Physics-informed neural networks: A deep learning framework for solving forward and inverse problems involving nonlinear partial differential equations. *Journal of Computational Physics*, pages 686–707, 2019. doi: 10.1016/j.jcp.2018.10.045.
- [36] Shengze Cai, Zhiping Mao, Zhicheng Wang, Minglang Yin, and

- George Em Karniadakis. Physics-informed neural networks (pinns) for fluid mechanics: a review. *Acta Mechanica Sinica*, pages 1727–1738, 2021. ISSN 0567-7718. doi: 10.1007/s10409-021-01148-1.
- [37] Pushan Sharma, Wai Tong Chung, Bassem Akoush, and Matthias Ihme. A review of physics-informed machine learning in fluid mechanics. *Energies*, 16(5):2343, 2023.
- [38] Zhiping Mao, Ameya D Jagtap, and George Em Karniadakis. Physics-informed neural networks for high-speed flows. *Computer Methods in Applied Mechanics and Engineering*, page 112789, 2020.
- [39] Elham Kiyani, Mahdi Kooshkbaghi, Khemraj Shukla, Rahul Babu Koneru, Zhen Li, Luis Bravo, Anindya Ghoshal, George Em Karniadakis, and Mikko Karttunen. Characterization of partial wetting by cmas droplets using multiphase many-body dissipative particle dynamics and data-driven discovery based on pinns. *Journal of Fluid Mechanics*, page A7, 2024.
- [40] Hamidreza Eivazi, Mojtaba Tahani, Philipp Schlatter, and Ricardo Vinuesa. Physics-informed neural networks for solving reynolds-averaged navier–stokes equations. *Physics of Fluids*, 2022.
- [41] Xiaowei Jin, Shengze Cai, Hui Li, and George Em Karniadakis. Nsfnets (navier–stokes flow nets): Physics-informed neural networks for the incompressible navier–stokes equations. *Journal of Computational Physics*, page 109951, 2021. ISSN 00219991. doi: 10.1016/j.jcp.2020.109951.
- [42] Hui Xu, Wei Zhang, and Yong Wang. Explore missing flow dynamics by physics-informed deep learning: The parameterized governing systems. *Physics of Fluids*, 33:095116, 2021. ISSN 1070-6631, 1089-7666. doi: 10.1063/5.0062377. URL <https://pubs.aip.org/pof/article/33/9/095116/1064746/Explore-missing-flow-dynamics-by-physics-informed>.
- [43] Maziar Raissi, Alireza Yazdani, and George Em Karniadakis. Hidden fluid mechanics: Learning velocity and pressure fields from flow visualizations. *Science (New York, N.Y.)*, pages 1026–1030, 2020. doi: 10.1126/science.aaw4741.
- [44] Shengze Cai, Zhicheng Wang, Frederik Fuest, Young Jin Jeon, Callum Gray, and George Em Karniadakis. Flow over an espresso cup: inferring 3-D velocity and pressure fields from tomographic background oriented schlieren via physics-informed neural networks. *Journal of Fluid Mechanics*, 915:A102, 2021. ISSN 0022-1120, 1469-7645. doi: 10.1017/jfm.2021.135. URL https://www.cambridge.org/core/product/identifier/S002211202100135X/type/journal_article.
- [45] Zhiping Mao, Ameya D. Jagtap, and George Em Karniadakis. Physics-informed neural networks for high-speed flows. *Computer Methods in Applied Mechanics and Engineering*, 360:112789, March 2020. ISSN 00457825. doi: 10.1016/j.cma.2019.112789. URL <https://linkinghub.elsevier.com/retrieve/pii/S0045782519306814>.
- [46] Sifan Wang and Paris Perdikaris. Deep learning of free boundary and Stefan problems. *Journal of Computational Physics*, 428:109914, March 2021. ISSN 00219991. doi: 10.1016/j.jcp.2020.109914. URL <https://linkinghub.elsevier.com/retrieve/pii/S0021999120306884>.
- [47] Aaron B. Buhendwa, Stefan Adami, and Nikolaus A. Adams. Inferring incompressible two-phase flow fields from the interface motion using physics-informed neural networks. *Machine Learning with Applications*, page 100029, 2021. doi: 10.1016/j.mlwa.2021.100029.
- [48] Lu Lu, Xuhui Meng, Zhiping Mao, and George Em Karniadakis. Deepxde: A deep learning library for solving differential equations. *SIAM Review*, pages 208–228, 2021. ISSN 0036-1445. doi: 10.1137/19M1274067.
- [49] Rundi Qiu, Renfang Huang, Yao Xiao, Jingzhu Wang, Zhen Zhang, Jiashun Yue, Zhong Zeng, and Yiwei Wang. Physics-informed neural networks for phase-field method in two-phase flow. *Physics of Fluids*, 2022. ISSN 1070-6631. doi: 10.1063/5.0091063.
- [50] Nanxi Chen, Sergio Lucarini, Rujin Ma, Airong Chen, and Chuanjie Cui. Pf-Pinns: Physics-Informed Neural Networks for Solving Coupled Allen-Cahn and Cahn-Hilliard Phase Field Equations, 2024. URL <https://www.ssrn.com/abstract=4761824>.
- [51] Sifan Wang, Xinling Yu, and Paris Perdikaris. When and why PINNs fail to train: A neural tangent kernel perspective. *Journal of Computational Physics*, 449:110768, January 2022. ISSN 00219991. doi: 10.1016/j.jcp.2021.110768. URL <https://linkinghub.elsevier.com/retrieve/pii/S002199912100663X>.
- [52] Alejandro Newell, Kaiyu Yang, and Jia Deng. Stacked hourglass networks for human pose estimation. In *Computer Vision – ECCV 2016*, Lecture Notes in Computer Science, pages 483–499. Springer International Publishing, Cham, 2016.
- [53] Salvatore Cuomo, Vincenzo Schiano Di Cola, Fabio Giampaolo, Gianluigi Rozza, Maziar Raissi, and Francesco Piccialli. Scientific machine learning through physics-informed neural networks: Where we are and what’s next. *Journal of Scientific Computing*, 2022. ISSN 0885-7474. doi: 10.1007/s10915-022-01939-z.
- [54] C.W Hirt and B.D Nichols. Volume of fluid (VOF) method for the dynamics of free boundaries. *Journal of Computational Physics*, 39(1): 201–225, January 1981. ISSN 00219991. doi: 10.1016/0021-9991(81)90145-5. URL <https://linkinghub.elsevier.com/retrieve/pii/0021999181901455>.
- [55] J.U Brackbill, D.B Kothe, and C Zemach. A continuum method for modeling surface tension. *Journal of Computational Physics*, pages 335–354, 1992. ISSN 00219991. doi: 10.1016/0021-9991(92)90240-Y. URL <https://linkinghub.elsevier.com/retrieve/pii/002199919290240Y>.
- [56] John W. Cahn and John E. Hilliard. Free Energy of a Nonuniform System. III. Nucleation in a Two-Component Incompressible Fluid. *The Journal of Chemical Physics*, pages 688–699, 1959. ISSN 0021-9606, 1089-7690. doi: 10.1063/1.1730447. URL <https://pubs.aip.org/jcp/article/31/3/688/76117/Free-Energy-of-a-Nonuniform-System-III-Nucleation>.
- [57] J. D. Van Der Waals. The thermodynamic theory of capillarity under the hypothesis of a continuous variation of density. *Journal of Statistical Physics*, pages 200–244, 1979. ISSN 0022-4715, 1572-9613. doi: 10.1007/BF01011514. URL <http://link.springer.com/10.1007/BF01011514>.
- [58] Pengtao Yue, James J. Feng, Chun Liu, and Jie Shen. A diffuse-interface method for simulating two-phase flows of complex fluids. *Journal of Fluid Mechanics*, pages 293–317, 2004. ISSN 0022-1120, 1469-7645. doi: 10.1017/S0022112004000370. URL http://www.journals.cambridge.org/abstract_S0022112004000370.
- [59] David Jacqmin. Calculation of Two-Phase Navier–Stokes Flows Using Phase-Field Modeling. *Journal of Computational Physics*, 155(1): 96–127, October 1999. ISSN 00219991. doi: 10.1006/jcp.1999.6332. URL <https://linkinghub.elsevier.com/retrieve/pii/S0021999199963325>.
- [60] Peter J. Huber. Robust Estimation of a Location Parameter. *The Annals of Mathematical Statistics*, pages 73–101, 1964. ISSN 0003-4851. doi: 10.1214/aoms/1177703732. URL <http://projecteuclid.org/euclid.aoms/1177703732>.
- [61] A. Ali Heydari, Craig A. Thompson, and Asif Mehmood. SoftAdapt: Techniques for Adaptive Loss Weighting of Neural Networks with Multi-Part Loss Functions, December 2019. arXiv:1912.12355 [cs].
- [62] Sokratis J. Anagnostopoulos, Juan Diego Toscano, Nikolaos Stergiopoulos, and George Em Karniadakis. Residual-based attention in physics-informed neural networks. *Computer Methods in Applied Mechanics and Engineering*, page 116805, 2024. ISSN 00457825. doi: 10.1016/j.cma.2024.116805.
- [63] Jin Xu, Zishan Li, Bowen Du, Miaomiao Zhang, and Jing Liu. Reluplex made more practical: Leaky relu. In *2020 IEEE Symposium on Computers and Communications (ISCC)*, pages 1–7. IEEE, 2020.
- [64] Ameya D. Jagtap, Kenji Kawaguchi, and George Em Karniadakis. Locally adaptive activation functions with slope recovery for deep and physics-informed neural networks. *Proceedings of the Royal Society A: Mathematical, Physical and Engineering Sciences*, 476(2239): 20200334, July 2020. ISSN 1364-5021, 1471-2946. doi: 10.1098/rspa.2020.0334. URL <https://royalsocietypublishing.org/doi/10.1098/rspa.2020.0334>.
- [65] Kaiming He, Xiangyu Zhang, Shaoqing Ren, and Jian Sun. Deep residual learning for image recognition, 2015.
- [66] Zhiqin Chen and Hao Zhang. Learning implicit fields for generative shape modeling. In *2019 IEEE/CVF Conference on Computer Vision and Pattern Recognition (CVPR)*, pages 5932–5941. IEEE, 2019.
- [67] Chen Cheng and Guang-Tao Zhang. Deep Learning Method Based on Physics Informed Neural Network with Resnet Block for Solving Fluid Flow Problems. *Water*, page 423, 2021. ISSN 2073-4441. doi: 10.3390/w13040423. URL <https://www.mdpi.com/2073-4441/13/4/423>.
- [68] Sifan Wang, Bowen Li, Yuhang Chen, and Paris Perdikaris. PirateNets: Physics-informed Deep Learning with Residual Adaptive Net-

- works, February 2024. URL <http://arxiv.org/abs/2402.00326>. arXiv:2402.00326 [cs, math].
- [69] Tijmen Tieleman and Geoffrey Hinton. Lecture 6.5-rmsprop: Divide the gradient by a running average of its recent magnitude. *COURSEERA: Neural networks for machine learning*, pages 26–31, 2012.
- [70] Maximilian Dreisbach, Sebastian Blessing, André Brunn, Frank Michaux, Alexander Stroh, and Jochen Kriegseis. Three-dimensional encoding of a gas–liquid interface by means of color-coded glare points. *Experiments in Fluids*, 64(3):53, 2023. ISSN 0723-4864. doi: 10.1007/s00348-023-03592-0.
- [71] H. C. van de Hulst. *Light scattering by small particles*. Dover books on physics. LSC Communications and Dover Publications, Inc, New York, unabridged and corrected republication of the work originally published in 1957 by john wiley & sons, inc., n.y edition, 1981.
- [72] Robert N. Wenzel. Resistance of solid surfaces to wetting by water. *Industrial & Engineering Chemistry*, pages 988–994, 1936.
- [73] Julius S. Bendat and Allan G. Piersol. *Random data : analysis and measurement procedures*. Wiley series in probability and statistics. Wiley, 4th ed (online-ausg.) edition, 2010.
- [74] Romain Rioboo, Cameron Tropea, and Marco Marengo. Outcomes from a drop impact on solid surfaces. *Atomization and Sprays*, pages 155–166, 2001.
- [75] Romain Rioboo, Marco Marengo, and Cameron Tropea. Time evolution of liquid drop impact onto solid, dry surfaces. *Experiments in Fluids*, pages 112–124, 2002.
- [76] Matthew Tancik, Pratul P. Srinivasan, Ben Mildenhall, Sara Fridovich-Keil, Nithin Raghavan, Utkarsh Singhal, Ravi Ramamoorthi, Jonathan T. Barron, and Ren Ng. Fourier features let networks learn high frequency functions in low dimensional domains. *NeurIPS*, 2020.
- [77] Sifan Wang, Hanwen Wang, and Paris Perdikaris. On the eigenvector bias of Fourier feature networks: From regression to solving multi-scale PDEs with physics-informed neural networks. *Computer Methods in Applied Mechanics and Engineering*, 384:113938, October 2021. ISSN 00457825. doi: 10.1016/j.cma.2021.113938. URL <https://linkinghub.elsevier.com/retrieve/pii/S0045782521002759>.